Development and Benchmarking of a Quasistatic d_{33}-meter for the Characterization of Piezoelectric Films and Nanostructures

Stefan Liccardi

Physics
2023-05

Master's Thesis

STUDENT REPORT

AALBORG UNIVERSITY

Title:
Development and Benchmarking of a Quasistatic d_{33}-meter for the Characterization of Piezoelectric Films and Nanostructures

Project Period:
Fall Semester 2022
to Fall Semester 2023

Author:
Stefan Liccardi

Supervisor:
Kjeld Pedersen

Copies: 3

Page Numbers: 57

Date of Completion:
December 14, 2023

Abstract:

This project goes through the design, development and characterization of an experimental setup used to measure piezoelectric coefficients.

The initial goal was to be able to characterize piezoelectric properties of nanoscale devices based on nitride nanowires. A setup intended to accomplish such measurements was designed based on the principles of Quasistatic measurement. A novel approach to force sensing was developed and tested to increase the signal quality during dynamic force measurements. The resultant experimental setup was then characterized to determine its viability as a platform for making various direct piezoelectric measurements. It did, however, suffer from issues related to time-dependent drift. The levels exceeded the anticipated levels owing to the relaxation of the sample itself. The exact reason for this effect needs to be investigated further. Additional testing and optimization is necessary to improve the accuracy to levels suitable for research purposes. It was demonstrated that a piezometer with at least mediocre accuracy could be constructed using common laboratory equipment.

Summary

This project goes through the design, development and characterization of an experimental setup used to measure piezoelectric coefficients.

The initial goal was to be able to characterize piezoelectric properties of nano-scale devices based on nitride nanowires. A setup intended to accomplish such measurements was designed based on the principles of Quasistatic measurements. Specifically, using the measurement scheme known as the Berlincourt method. A novel approach to force sensing was developed to increase the signal quality of dynamic force measurements. The fundamental theory and dealing with the measurement of piezoelectric coefficients has been described.

The resultant experimental setup was then characterized to determine its viability as a platform for conduction various direct piezoelectric measurements. It did, however, suffer from issues related to time-dependent drift. The levels exceeded the anticipated levels owing to the relaxation of the sample itself. The exact reason for this effect needs to be investigated further.

In order to improve accuracy to levels suited for research purposes, additional testing and optimization is necessary. It was demonstrated that a highly customizable piezometer with at least mediocre accuracy could be constructed using common laboratory equipment.
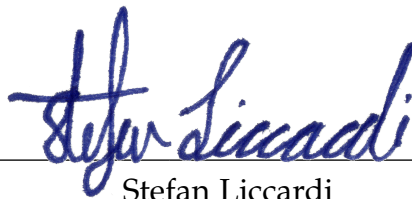
Contents

Preface

This is the Master's Thesis written by me, Stefan Liccardi, as the final part of my master's degree in Physics. Work began in the summer of 2022, and has concluded in December 2023. I would like to express my gratitude and appreciation to the many people in the department who have assisted me during the writing of this project. References are denoted by $[n]$ or $^{[n]}$ where n refers to the number in the bibliography.

<div align="right">Aalborg University, December 14, 2023</div>

_____

Stefan Liccardi

slicca18@student.aau.dk

Chapter 1

Introduction

Piezoelectric materials are at the foundation of many technologies. Quartz based piezoelectric crystal resonators provided the first stable frequency references paving the way for reliable electrical watches, long-range radio communication and computing devices. The discovery of piezoelectric ceramics led to the widespread adoption of piezoelectric sensors in commercial and consumer devices. In recent years, research in nanostructured piezoelectric materials has led to a renewed interest in the development of characterisation methods for the purpose of evaluating their efficacy.[1] Specifically, the prospect of using nanostructured piezoelectric materials as the basis of nano-scale energy generators has been of great interest. Proposed applications include biomechanical sensors and self-powered electronic devices.[2] Similarly, The development of piezoelectric films is of interest, due to their many uses in the development of MEMS devices[3] and for their applications in next-generation wireless communication systems.[4]

The development of a low-cost and low-complexity measurement system suitable for the measurement of the piezoelectric activity of diverse sets of samples, ranging from bulk piezoelectric single crystals to nanostructured piezoelectric devises, is highly desirable. This project focuses on the development, construction, and characterisation of exactly such a system.

Overview of the Report

This report is intended to describe both the practical and theoretical considerations relevant to the construction of a Quasistatic piezometer. It will also present the capabilities of the resultant measurement system. Chapter 2 Goes through the relevant theory needed to understand the choices and considerations made while developing the setup. It covers the fundamental mechanics of materials, the piezoelectric effect, and summarizes typical approaches to the measurement of piezoelectric coefficients. Chapter 3 Covers the devel-

opment and design of the experimental setup. Lastly, Chapter 4 presents experimental results obtained using the system in order to describe the characteristics of the meter and to benchmark the capabilities of the measurement system.

Chapter 2

Introduction to the piezoelectric effect, and measurement of piezoelectric coefficients

We will now introduce the fundamental theory necessary to describe the piezoelectric effect and the theory relevant to the process of measuring a material's piezoelectric coefficients. Since the piezoelectric effect is an electro-mechanical coupling, a general description of materials subject to mechanical loading will be presented.

2.1 Material Mechanics

We will start by considering a slab of a given isotropic material uniformly supported underneath and subject to a normal compressive load F, distributed homogeneously over the top A of the slab.
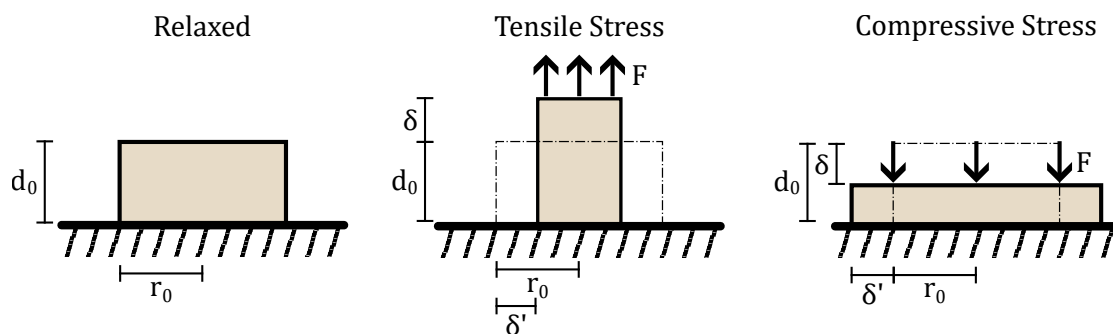

Figure 2.1: A uniformly loaded slab, under tensile and compressive stress. Along with its associated deformation.

Then the stress σ is defined as the force per unit area:[5]

$$\sigma = F/A. \tag{2.1}$$

This leads to a deformation δ in the thickness d_0 of the slab. Then, the strain ϵ is defined as the elongation per unit length:[5]

$$\epsilon = \delta/d_0, \tag{2.2}$$

such that the strain is negative if the material is under compression and positive when under tension. Hence, in the linear-elastic regime the stress and strain are related by Hooke's law:

$$\sigma = E\epsilon, \tag{2.3}$$

where the material constant of proportionality E is known as Young's Modulus. The elongation in one material direction is coupled with a contraction in the other material directions (see Figure 2.1) and the ration of normal strain and lateral strain ϵ', are related by Poisson's Ratio ν:

$$\nu = -\epsilon'/\epsilon. \tag{2.4}$$

When considering common isotropic materials subject to forces not exceeding their elastic limits, the above description is typically sufficient.

2.2 Tensor Formulation for the Mechanics of Isotropic and Anisotropic Materials

We will now generalize the previous section to define the stress and strain at any material point in both isotropic and anisotropic materials. This is typically done by the introduction of a tensor formalism to describe the material properties and states of the material points.

2.2.1 Displacement and Strain

For the purpose of generalizing the concept of strain, we must briefly discuss how to handle the deformation of a continuous material body. We do this by introducing the formalism of material points and actual positions. We consider a body in its relaxed state, each point in the material can be described by a position vector:[6]

$$\boldsymbol{X} = (X_1, X_2, X_3). \tag{2.5}$$

Applying a load to the material results in the deformation of the material. We denote the position of the material point X after deformation by its actual position $\boldsymbol{x}$, such that it is a

function of the material point and time:

$$x = x(X, t). \tag{2.6}$$

We note that an inverse function must exist such that you can find the material point inhabiting any actual position at any time: $X = X(x, t)$. In component form, the relations read[6]

$$x_i = x_i(X_k, t), \tag{2.7}$$
$$X_i = X_i(x_k, t). \tag{2.8}$$
$$\tag{2.9}$$

We refer to X_i as material coordinates and to x_i as spatial coordinates. We assume that each of the resultant functions are partially differentiable with respect to all material or spatial coordinates. Then displacement u of material point X is given as[6]

$$u_i = x_i - X_i. \tag{2.10}$$

On this basis and through a rather laborious calculation not relevant for our purposes (See [7]), the strain in eq. (2.2), can be generalized to tensor form:

$$S_{kl} = \frac{1}{2} \left(\frac{\partial u_k}{\partial X_l} + \frac{\partial u_l}{\partial X_k} \right). \tag{2.11}$$

In the case of normal strains S_{ii} it simply reduces to $S_{ii} = \frac{\partial u_i}{\partial X_i}$. This is equivalent to equation (2.2). In the case of shear strains, S_{kl}, the above definition represents half of the angle deformation relative to the right angles in the reference configuration. Hence, it is obvious that the strain tensor is symmetric:[6]

$$\overset{=}{S} = \begin{pmatrix} S_{11} & S_{12} & S_{13} \\ S_{12} & S_{22} & S_{23} \\ S_{13} & S_{23} & S_{33} \end{pmatrix}. \tag{2.12}$$

2.2.2 The Cauchy Stress Tensor

To generalize the concept of stress, (2.1), we consider an infinitesimal surface located at a material point P. The surface can be any arbitrary surface within the material, real or imagined. Its unit normal vector n can be written as a linear combination of the unit vectors e_i of the coordinate system:[6]

$$n = n_1 e_1 + n_2 e_2 + n_3 e_3. \tag{2.13}$$

Each infinitesimal surface normal to the unit vectors e_i has an associated stress vector $t^{(i)}$, encompassing both normal and shear stresses. Hence, the stress vector t associated with the surface normal to $\hat{n}$, can be expressed as the linear combination[6]

$$t = t^{(1)}n_1 + t^{(2)}n_2 + t^{(3)}n_3. \tag{2.14}$$

Hence, we can describe the stress using the Cauchy stress tensor $\overset{\rightleftharpoons}{T}$, using the following relation:[6]

$$t = \overset{\rightleftharpoons}{T}n, \tag{2.15}$$

where the contribution to the t_i component of the stress vector due to the stress on n_k is given by:[6]

$$t_i = T_{ik}n_k. \tag{2.16}$$

Then, in matrix form $\overset{\rightleftharpoons}{T}$ is the second rank tensor written as

$$\overset{\rightleftharpoons}{T} = \begin{pmatrix} T_{11} & T_{12} & T_{13} \\ T_{21} & T_{22} & T_{23} \\ T_{31} & T_{32} & T_{33} \end{pmatrix}.$$

Here the components T_{ii} are normal stresses, and the components T_{jk} are shear stresses. $\overset{\rightleftharpoons}{T}$ is symmetric. The full derivation can be found elsewhere ([7]), but it can be intuitively understood by considering that stress must be assigned to a material element in equilibrium. Hence, each normal stress must be opposed by an equal normal stress on the opposing surface. Similarly, shear stresses result in a torque that must be opposed to maintain equilibrium. Therefore,

$$T_{ik} = T_{ki}. \tag{2.17}$$

This reduces the Cauchy stress tensor to 6 independent elements completely describing the stress at a material point:[6]

$$\overset{\rightleftharpoons}{T} = \begin{pmatrix} T_{11} & T_{12} & T_{13} \\ T_{12} & T_{22} & T_{23} \\ T_{13} & T_{23} & T_{33} \end{pmatrix}. \tag{2.18}$$

2.2.3 Hooke's Law in Tensor Notation

Now, that the concepts of strain and stress have been described in tensorial form. We can state Hooke's Law (equation (2.3)) in tensor form:[6]

$$T_{ij} = c_{ijkl}S_{kl}. \tag{2.19}$$

Here, the material constants of proportionality c_{ijkl} are analogous to Young's modulus and are called elastic stiffnesses. Equivalently, it can be stated as the inverse:[6]

$$S_{ij} = s_{ijkl}T_{kl}, \tag{2.20}$$

where s_{ijkl} are referred to as elastic compliances.

2.3 Index Notation for Piezoelectric Materials

As the last preliminary before turning our attention to describing the piezoelectric effect, we will briefly summarize the relevant notation conventions for directions in piezoelectric crystals.

2.3.1 Compressed Tensor Index Notation

When describing piezoelectric materials it is standard to introduce a contracted notation such that index pairs ij or kl, are replaced by singular indices λ or μ:[8]

$$
\begin{array}{ccc}
ij \text{ or } kl & \rightarrow & \lambda \text{ or } \mu \\
\hline
11 & \rightarrow & 1 \\
22 & \rightarrow & 2 \\
33 & \rightarrow & 3 \\
23 \text{ ; } 32 & \rightarrow & 4 \\
31 \text{ ; } 13 & \rightarrow & 5 \\
12 \text{ ; } 21 & \rightarrow & 6
\end{array}
\tag{2.21}
$$

When moving to this notation, we make the following simple substitution for the stress tensor:

$$
\begin{pmatrix} T_{11} & T_{12} & T_{13} \\ T_{21} & T_{22} & T_{23} \\ T_{31} & T_{32} & T_{33} \end{pmatrix} = \begin{pmatrix} T_1 & T_6 & T_5 \\ T_6 & T_2 & T_4 \\ T_5 & T_4 & T_3 \end{pmatrix}.
$$

Considering shear strains, we expand the compressed notation to include the entire angle deformation, such that

$$
\begin{pmatrix} S_{11} & S_{12} & S_{13} \\ S_{21} & S_{22} & S_{23} \\ S_{31} & S_{32} & S_{33} \end{pmatrix} = \begin{pmatrix} S_1 & \frac{1}{2}S_6 & \frac{1}{2}S_5 \\ \frac{1}{2}S_6 & S_2 & \frac{1}{2}S_4 \\ \frac{1}{2}S_5 & \frac{1}{2}S_4 & S_3 \end{pmatrix}.
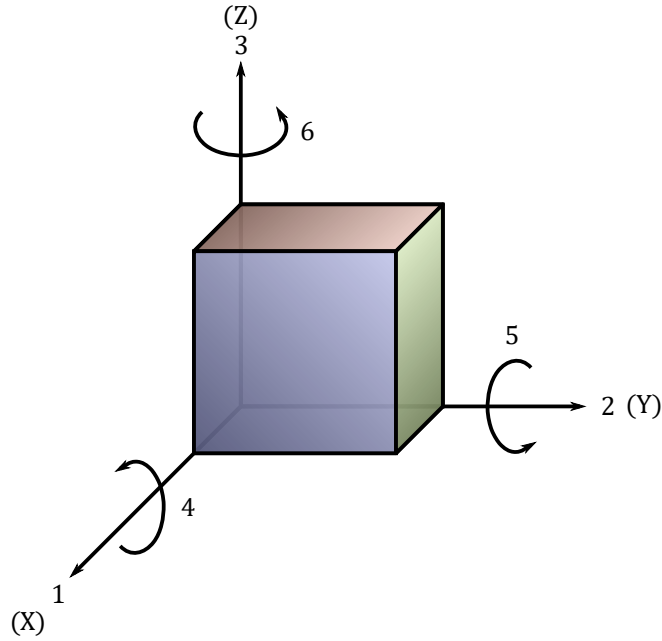$$

Figure 2.2: The directions defined by the contracted index notation.

When $\lambda \in \{4,5,6\}$, this results in the value S_λ encompassing the total angle deformation in one plane. Hence, the equations (2.19), and (2.20) can be rewritten as

$$T_\lambda = c_{\lambda\mu}S_\mu, \tag{2.22}$$
$$S_\lambda = s_{\lambda\mu}T_\mu, \tag{2.23}$$

and be understood to include the relevant totals of normal and shear strains. A schematic representing the compressed index notation can be seen in figure 2.2.

2.3.2 Conventions for Describing Directions in Piezoelectric Crystals

The index notation ij, kl and in turn λ, μ is based on a Cartesian coordinate system. The directions denoted by $i, j, k, l \in \{1, 2, 3\}$ map directly to the x-, y-, and z-axis, such that

$$\hat{x} = e_1, \quad \hat{y} = e_2, \quad \hat{z} = e_3.$$

This convention is convenient when working with a sample in an experimental setup, but leaves the issue of defining how the Cartesian axes are oriented relative to the crystallographic axes. This mapping is usually made using a set of general conventions for each of the 7 crystal systems and by specific assignments, depending on the point group and material properties. Throughout this rapport, axis notation will follow the conventions described in the IEEE Standard on Piezoelectricity [8]. The relevant axis assignment will be described later when new material samples are discussed.

2.4   The Piezoelectric Effect

The piezoelectric effect is an electromechanical coupling, resulting in a material developing an electric polarization as the result of an applied stress. Historically, this is referred to as the direct piezoelectric effect. The effect depends strongly on the symmetry of the crystal, and it typically occurs only in crystals without a centre of symmetry. Phenomenologically, the direct piezoelectric effect in noncentrosymmetric crystals can be explained, by considering the displacement of ions in the unit cell due to the applied stress. This leads to the generation of electric dipoles in the lattice inducing a polarization.[9] The direct piezoelectric effect can be expressed as

$$P = \overleftrightarrow{d}\,\overleftrightarrow{T},\tag{2.24}$$

where P is the vector describing the electric polarization due to the applied stress and $\overleftrightarrow{d}$ is the piezoelectric charge tensor containing the piezoelectric charge coefficients.

In component form, this can be written as [10]

$$P_i = \sum_{j,k} d_{ijk} T_{jk},\tag{2.25}$$

where $x, y, z = i, j, k$

The convention for the sign of the piezoelectric coefficient is adopted according to [8]. Thus, the piezoelectric coefficient d_{33} is defined as positive when an applied tensile stress parallel to the Z-axis results in a potential difference with the positive terminal on the +Z face (see Figure 2.3). The indirect effect (also known as the converse effect) is described as the induced strain due to an applied external electric field and can be described by[10]

$$S_{jk} = \sum_{i} d_{ijk} E_i,\tag{2.26}$$

where S_{jk} are components of the strain tensor $\overleftrightarrow{S}$.

2.5   Linear Dielectrics and Piezoelectricity

The electric displacement D of a dielectric material is defined by

$$D = \epsilon_0 E + P.\tag{2.27}$$

Materials in which the polarization is linearly proportional to the electric field are called linear dielectrics. The quantities are related by the proportionality constant $\overleftrightarrow{\chi}$ called the
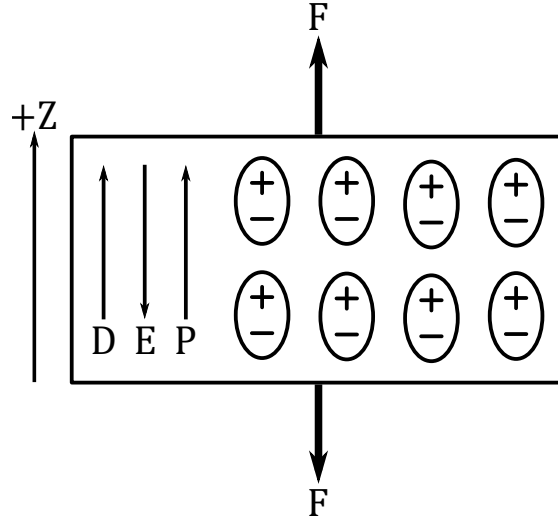
Figure 2.3: Piezo electric sample with positive d_{33} under tension. Shown is the polarity of the induced dipoles and the directions fields.

electric susceptibility. In isotropic media this can be written as[11]

$$\boldsymbol{P} = \epsilon_0 \chi \boldsymbol{E}. \tag{2.28}$$

Hence, in component form, from equation (2.27):

$$D_i = \epsilon_0 E_i + \epsilon_0 \chi E_i = \epsilon_0 (1 + \chi) E_i, \tag{2.29}$$

such that the electric displacement is proportional to the electric field

$$D_i = \epsilon E_i, \tag{2.30}$$

where $\epsilon = \epsilon_0 (1 + \chi)$ is the electric permittivity tensor. Lastly, the dielectric permittivity is defined as the ratio of the permittivity and vacuum permittivity:

$$\epsilon_r = \frac{\epsilon}{\epsilon_0} = (1 + \chi). \tag{2.31}$$

Generally, the dielectric permittivity can be expanded to tensor notation such that it can also describe anisotropic media: [6]

$$\varepsilon_{ik} = \frac{\partial D_i}{\partial E_k}. \tag{2.32}$$

Including the piezoelectric contribution (2.24) to the displacement field yields

$$\boldsymbol{D} = \overleftrightarrow{\epsilon}^T \boldsymbol{E} + \overleftrightarrow{d} \overleftrightarrow{T}, \tag{2.33}$$

where the superscript T denotes the dielectric permittivity at constant stress.

Now, the piezoelectric coefficient can be determined from equation (2.33) by considering the differential while maintaining constant electric field:

$$d_{i\mu} = \left[\frac{\partial D_i}{\partial T_\mu}\right]_E . \tag{2.34}$$

This leads to the ability to practically measure the piezoelectric coefficient of a material directly.[1]

2.6 Approaches to Measurement of Piezoelectric Coefficients

For the purpose of the following discussion, we adopt a general notation of piezoelectric coefficients in which d_{33} refers to any piezoelectric coefficient as measured at normal stresses. Similarly, the notation d_{31} is used to refer to transverse coefficients measured at stresses perpendicular to the contact faces. Many approaches to the determination of the piezoelectric coefficient have been developed. The simplest of which, is measuring the d_{33} coefficient directly using the piezoelectric effect, often referred to as the normal loading method. A normal compressive stress is applied to the piezoelectric sample and the resultant charge is measured on the faces normal to the axis of loading. In practice, this is done by placing the sample between two metal contacts and mechanically loading one of the contacts. This offers the obvious advantage of being flexible in implementation, making it possible to measure samples of differing geometries with relative ease. Accuracy of the measured d_{33} is typically limited by the ability to ensure uniform loading across the contact interface.[12]

Measuring the d_{31} coefficient can be achieved by inducing a known displacement. The sample is mounted as a cantilever and it is bent by loading the free end of the beam. Since this can induce large displacements, it is feasible to calculate d_{31} based on the elastic compliances of the material and the displacement at the free tip of the beam.

Many variations on measuring the piezoelectric coefficient by direct mechanical loading exist and they generally differ in their approach to applying and sensing force.[12] As an illustration of the wide variety of possible schemas; a recent approach ([13]) uses an air stream from a pneumatic airgun to measure d_{33}.

The converse piezoelectric effect has also been utilised to measure piezo electric coefficients. Typically, the sample is excited by applying an electric field and the induced deformation is measured using an interferometer.

---

[1]A similar approach can be used to find a relation for the inverse piezoelectric effect by considering contributions to the total strain: $S = \overset{\leftrightharpoons}{s}^E \overset{\leftrightharpoons}{T} + \overset{\leftrightharpoons}{d} E$, where $\overset{\leftrightharpoons}{s}^E$ is the compliance tensor at constant electric field.

Lastly, measurement of piezoelectric coefficients using resonance methods is also common. They require a sample with a geometry that is known to a high degree. And in these cases, they offer high precision.[9]

The high degree of flexibility inherent in the normal loading measurements schemas makes them practical as a means of benchmarking during piezoelectric material development.

2.6.1   Quasistatic Measurement of Piezoelectric Coefficients

Thermal effects lead to a drift of charges over time when a piezoelectric material is loaded with a static force. This reduces the precision of the measurements. The dominant approach to reduce this effect is to make these measurements using a low frequency alternating force. The frequency should be low enough to reasonably assume a static mechanical equilibrium at all times during measurement. In this scenario, we refer to the measurement as being quasistatic. The common quasistatic normal loading measurement schema is called the Berlincourt Method.[9]
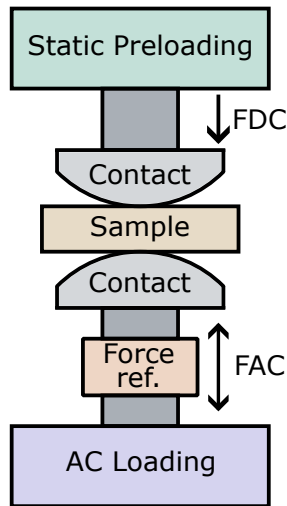

Figure 2.4: Overview of a Quasistatic Berlincourt type $d_{33}-$meter.

To distinguish between static and alternating forces, we will use a minor bastardisation of the nomenclature for direct current and alternating current electrical signals to refer to the type of force associated with a measurement: A DC force should be read as a static force, and an AC force should be understood as the component of the force which varies during quasistatic measurement.

The fundamentals of the d_{33} measurement procedure follows from considering equation (2.34). A uniaxial stress can be expressed simply by equation (2.1). Supposing that the ratio of the sample's thickness to its width is sufficiently low. We can assume that the piezoelectric contributions to measured charge are solely due to the stress in the Z-direction.[14]

The dielectric displacement can be expressed based on the assumption of a uniform charge distribution across the sample surface. Then, $D = Q/A$ where A is the surface area of the interface of sample and contact. This leads to the convenient attribute of a Berlin court type meter, namely that the piezoelectric charge coefficient is independent of the surface area of the sample. [9]

$$d_{i\mu} = \left[\frac{\partial Q/A}{\partial F/A}\right]_E = \left[\frac{\partial Q}{\partial F}\right]_E . \tag{2.35}$$

It should be emphasized that the resultant d_{33} of a Berlincourt type measurement is solely dependent on the applied force and the measured charge. For as long as the aspect ratio of the sample remains low at all points and that both faces and all edges can be assumed to be parallel, the sample can be measured using the meter. Also note that equation (2.35) requires that measurements be done at short-circuit conditions. We will discuss how this is achieved in Chapter 3.

An overview of the mechanical components of a typical Berlincourt type meter is shown in Figure 2.4. The AC force is applied using a linear mechanical actuator. To ensure the sample remains in place and in contact with the contact probes during measurement, a static preload is applied using some form of clamping system. An inline force reference is usually included to quantify the AC forces. This type of referencing can be done either using an actual force transducer giving direct readings of the applied force, or by using a well characterized piezoelectric reference sample as a means of comparison. If using a reference sample, the output of the measured d_{33} can be calculated simply using

$$d_{33sample} = Q_{sample}/F, \quad d_{33ref} = Q_{ref}/F$$
$$\Rightarrow d_{33sample} = \frac{Q_{sample}}{Q_{ref}} d_{33ref}.$$

The predominant challenge with this type of force calibration is choosing a stable reference sample. That is, it should be stable across the entire frequency, force, and preload range of the setup. Ideally, such a reference must also be highly piezoelectric to increase the signal-to-noise ratio of the referencing system.

The metallic contact probes are typically rounded. This is intended to reduce contact issues related to the roughness of the sample. Furthermore, mismatches in Poisson's ratios between sample and metal contact, lead to additional lateral strain contributions in measured charge. A large flat contact increases the coupling of lateral strains to the sample.[14]

Chapter 3

Design and Construction of a Quasistatic Meter

Throughout this project, much time and consideration has gone into the design and construction of a homemade method of measuring piezoelectric coefficients of various samples. This development is the main aim of this project. Specifically, the setup should be able to accommodate samples of differing dimensions and geometries. Additionally, the setup should be easy to modify and reconfigure, such that it can be customized to make measurements requiring non-standard sample mounting and probing. Hence, the system is made up of a collection of modular component assemblies that can be changed or reconfigured non-destructively. This requirement is also reflected in material and component choice. Throughout the development and testing process I have, with very few exceptions, made parts using materials common to a university machine shop. Homemade structural components have, whenever possible, been made using materials that are easy to machine such as aluminium, brass, delrin or nylon. For the amateur machinist this offers the twofold benefit of making a replication of the setup as easy as possible, and reducing component variability due to the simplification of machining processes. I should, however, emphasise that these choices do not in most cases represent the optimal solutions when solely considering the material properties of the components in the context of the measurement system. Most electronic components and devices used in the system are also commonly available in any electronics lab and somewhat rarer components have been chosen such that they are commonly stocked by major electronics suppliers. Hence, it should be possible to construct an improved or customized system on the basis of the design considerations presented in this report. The impetus of the design was to develop a method of measuring the piezoelectric coefficients of piezoelectric nanostructures grown on flat wafers. This goal has guided several of the minute design decisions. I have, however, not been able to get a hold of such samples and have therefore not been able to confirm its
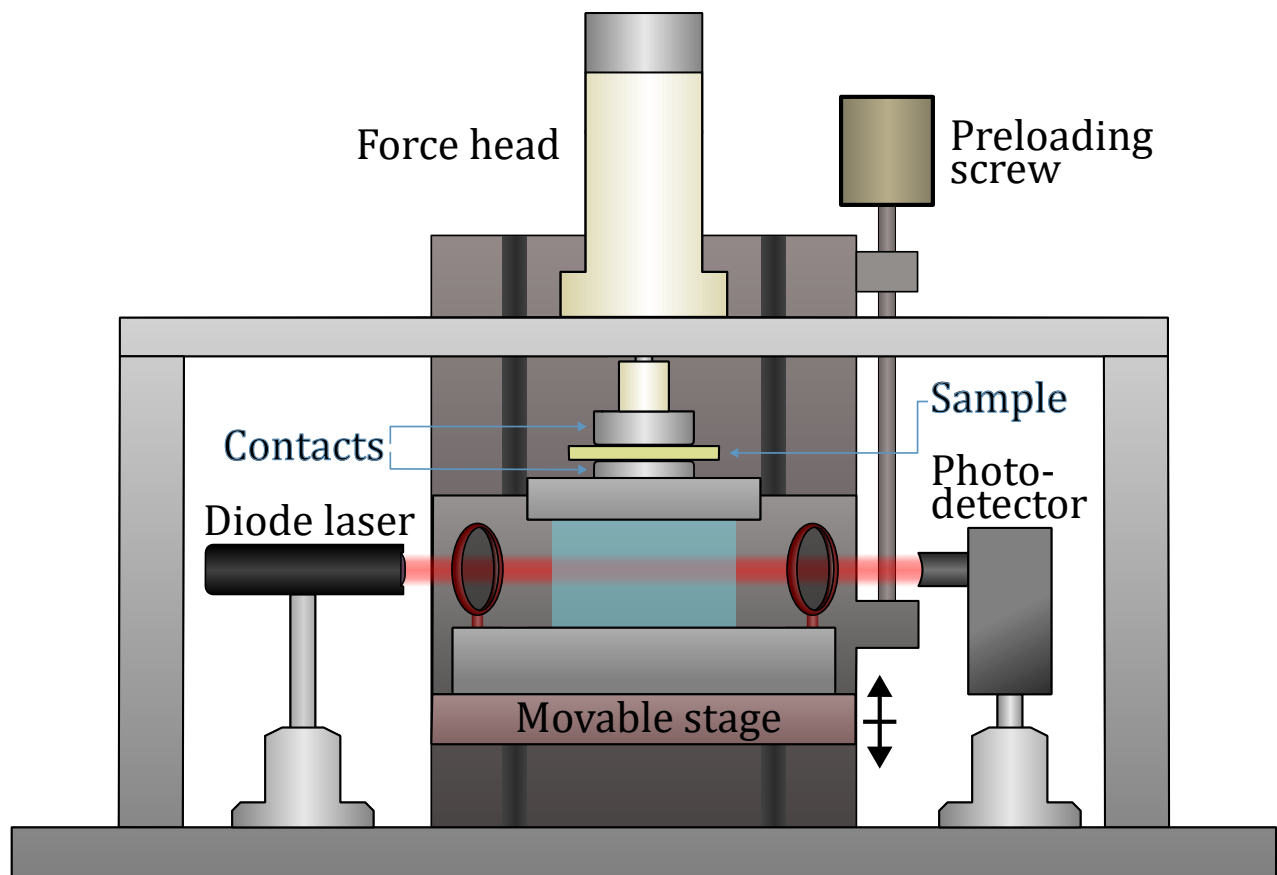
Figure 3.1: Overview of the physical construction of the experimental setup.

viability in these cases.

3.1 Overview of the Experimental Setup

The resultant setup is based on the principles of a Berlincourt meter discussed in Section 2.6.1. Hence, it uses a normal loading scheme, and applies an AC load to conduct measurements quasi-statically. Consider the schematic overview of the experimental setup, which can be seen in Figure 3.1. The core setup can be divided into 4 functionally separate systems:

1. The sample mounting and preloading system

2. The AC Loading system

3. The force referencing system

4. The sample probing and charge measurement system

Although functionally separate, the systems are not self-contained and their individual components may serve multiple purposes in multiple systems. Additional support systems are needed to successfully make a measurement. These are rarely discussed in the literature but, in practice, decisions in the choice of their design and components have had a significant impact on the quality of the acquired data. The support systems include:

1. The measurement control system

2. The force calibration system

3. The data acquisition system

4. The data processing system

The setup is built on top of a thick aluminium plate. A movable stage is mounted in the middle of the plate. The stage provides Z-axis adjustment. On the stage itself, the force sensor and bottom sample contact are mounted. An aluminium beam is mounted above the stage supported by two aluminium legs. This beam supports the force head which is home to the AC loading system and force calibration components. The top sample contact is mounted on the bottom of the force head. The force sensor is based on optical sensing. Therefore, optical components are mounted on the stage and on both sides of the stage, the largest of which are a diode laser and a photodetector. We will now go through the individual systems in appropriate detail.

3.2   Sample Mounting and Loading Systems

The system applies AC force using a piezoelectric actuator. The specific actuator was taken from a common micrometer screw assembly commonly found in optics labs. This also makes it possible to use a typical piezoelectric controller to drive the actuator. The actuator itself is mounted in a custom machined plastic holder. This serves to align the actuator to the sample holder and force sensor. The top of the actuator is supported by a metal pin which couples the actuator to a compressive load cell.

The sample is mounted between two cylindrical aluminium contacts, both having flat faces at the sample contact interfaces. The sample is clamped in place by adjusting the position of the stage. This makes it possible to accommodate samples of varying thicknesses. This also sets the level of DC load. The level of DC load can then be read directly from the output of the reference load cell.
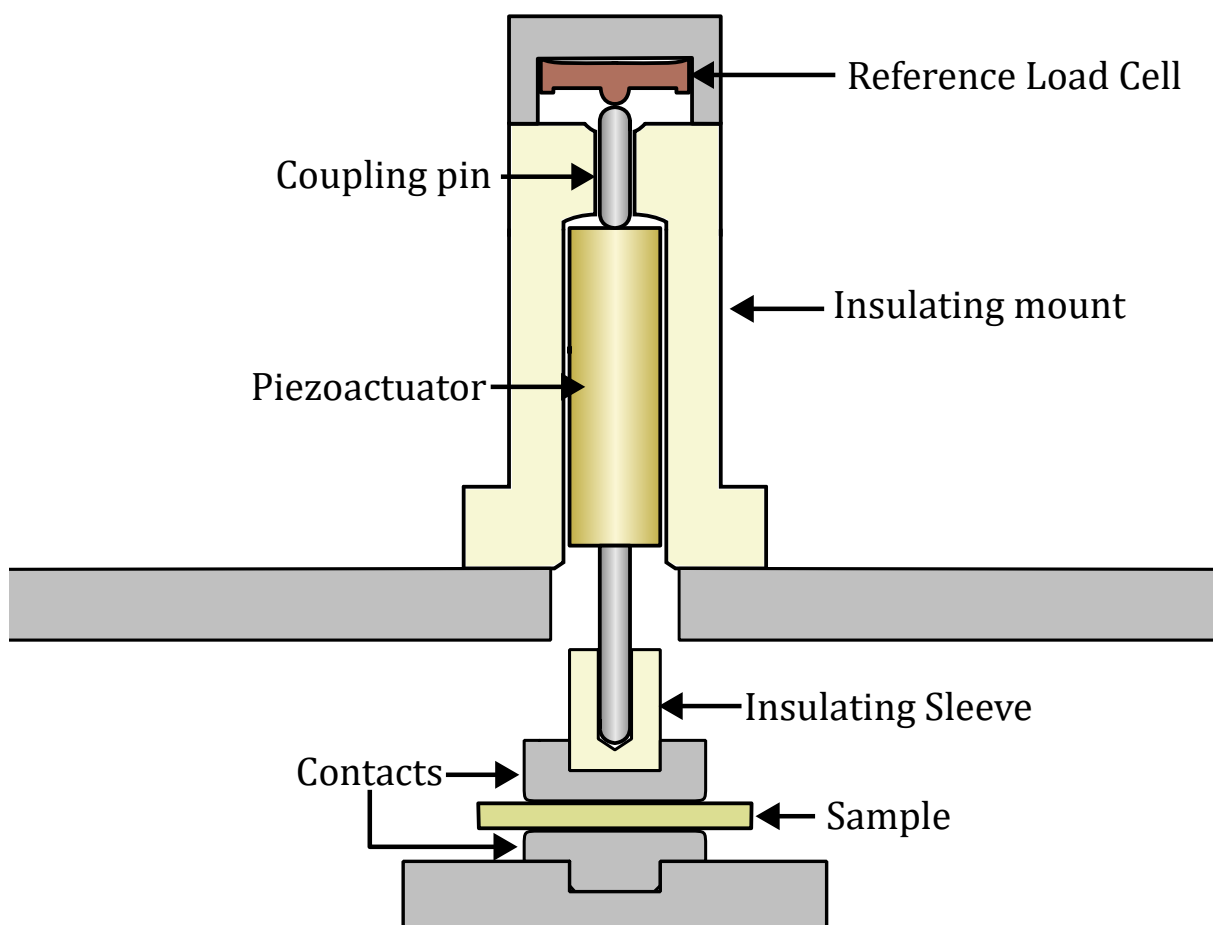
Figure 3.2: Cross-section of the forcehead and sample mounting system.

The flat contact geometry was chosen despite common practice, since the manual fabrication and alignment of two matching rounded contacts is inherently difficult. The fabrication of uniform flat contacts is comparatively simpler and the effect of transverse alignment errors is greatly reduced.

The actuator is insulated from the rest of the setup using the two insulating components seen in Figure 3.2. This also insulates the top contact from the frame of the system. The bottom contact is also insulated, here through non-conductive components in the force sensor.

The Reference Load Cell

The reference load cell can provide readings of loads up to $45N$, and can withstand up to $110N$.[1] This is what places the upper limit on the readable preload. In the unlikely case that larger preloads are required, the load cell can be removed and the coupling pin can be replaced with a longer pin.

The load cell provides output digitally over I^2C. This can be read using an ordinary Arduino microcontroller and transmitted over serial to the setup's control system. This greatly simplifies its integration and also comes with the added benefit of including factory calibration and temperature compensation. The accuracy of the calibration was confirmed using calibration weights before installation. The drawback of this digital approach is that readings are too slow to effectively sample the AC forces. Therefore, another force reference is needed.

3.3   Force Measurement

This system is designed to measure the AC force directly, rather than using an inline reference. This was primarily done as a way to reduce the impact of electrical noise in the force referencing system. Precision charge measurements are susceptible to many sources of electrical noise. This is in practice very difficult to control and predict. Secondly, using a piezoelectric reference sample also introduces issues related to its stability over time and over different measurement parameters. If measuring similar samples, this can serve as a compensation mechanism but since the setup is intended to measure various sample types, we should not assume a specific piezoelectric reference as a valid analogue.

The first iteration of the sensor was based on measuring the deformation of a thin beam on which the piezoelectric actuator was mounted. This was done using 4 matching strain gauges mounted on the beam. The strain gauges were connected to a Wheatstone bridge in the half bridge configuration. The output of the bridge was amplified using a typical

---

[1]Specifically, the load cell is a TE Connectivity Model: FX29-K0100A–0010–L [15]
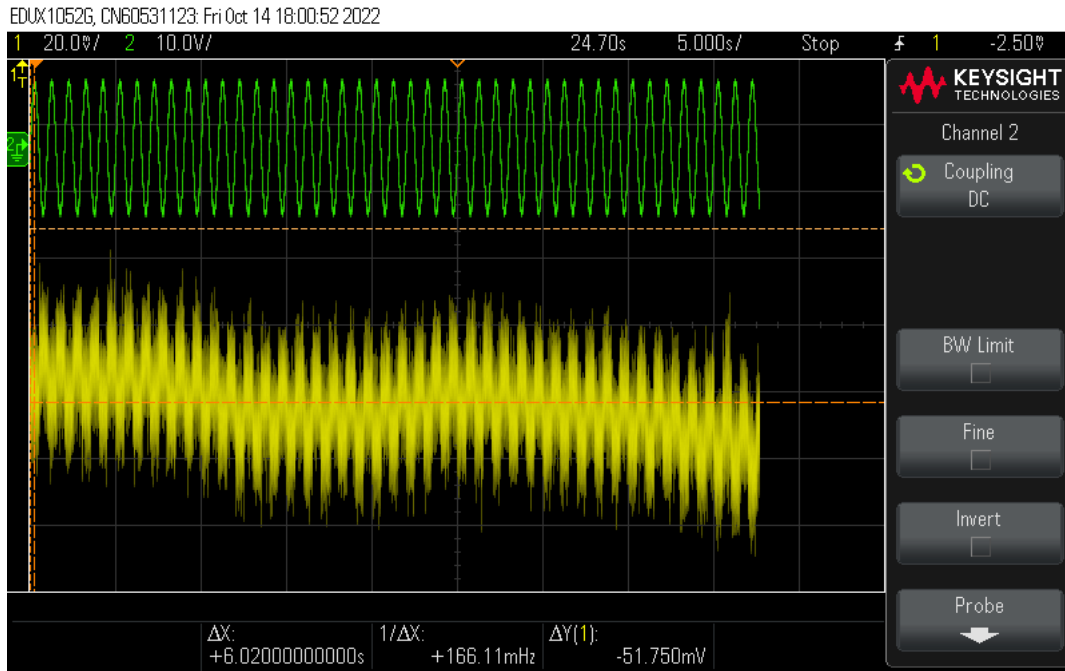
Figure 3.3: Screen grab from the oscilloscope showing the signal from the strain gauge based force sensor. Channel 1 (shown in yellow) is the signal from the strain gauge sensor and Channel 2 (shown in green) is the control signal controlling the piezoelectric actuator.

instrumentation amplifier circuit. The resultant signal had a poor signal-to-noise ratio (see Figure 3.3) and despite multiple attempts at amplification and signal conditioning it never produced a viable signal. Due to the problem with electrical noise, an alternate approach was needed. This led to the development of an optical force sensor based on the photoelastic effect.

3.3.1   Optical Force Sensing

The idea of implementing optical force detection was based on the desire to reduce the impact of electrical noise in the force sensing apparatus. Quite simply, we want to avoid the problem of detecting a small electrical signal from an electrical sensor mounted in the force head of the system. Using a conventional analogue load cell inline with the loading system, it requires introducing an amplifier into the immediate vicinity of the piezoelectric sample. This introduces an unnecessary source of electrical noise close to the sensitive charge measurement apparatus. Alternatively, it requires long cable runs which themselves are prone to picking up electrical noise.

By placing an optical intensity modulator in the load train instead, the force can be detected by measuring the changes in the intensity of a laser beam. Assuming that an

optical modulator of sufficient sensitivity can be constructed and mounted inline with the loading system, the optical signal can be guided from the modulator to a photodetector placed relatively far away with effectively no increase in the signal noise. Thus, removing the need to place noisy electronics near the sample. Additionally, amplification can then be done directly in the circuitry of the photodetector, essentially eliminating the electrical noise due to cabling.

3.3.2 Photoelastic Force Detection

This leads us to the development of a low noise optic force transducer based on the photoelastic effect. The photoelastic effect describes the tendency of some materials to become birefringent when strained. That is an ordinarily optical isotropic material with refractive index n_0, experiencing an anisotropic change in refractive index due to being strained. Disregarding shear stresses, the linear change in refractive index in direction i due to an applied stress is given by[16]

$$n_i - n_0 = c_1 T_{ii} + c_2 (T_{jj} + T_{kk}),$$ (3.1)

where the material dependant coefficients c_1 and c_2 are referred to as stress optic coefficients. Hence, asymmetrical loading of the material, results in a relative difference between the refractive indices. This is what is called birefringence. This difference can be expressed by

$$n_i - n_j = (T_{jj} - T_{ii})(c_2 - c_1).$$ (3.2)

Now consider a linearly polarized monochromatic beam normally incident upon the ij-plane of a loaded photoelastic material with length L. The relative phase of the i any j components of the incident light after exiting the photoelastic material is given by

$$\Delta\phi = \frac{2\pi}{\lambda} L(n_2 - n1).$$ (3.3)

This component dependent phase shift leads to the light being elliptically polarised after exciting the photoelastic media. This phase shift is, quite conveniently, directly proportional to the applied load. This effect can be measured by placing the photoelastic material between a pair of crossed linear polarizers. When no stress is applied, the beam intensity after the second polariser is zero. However, when a stress is applied to the photoelastic media, the beam's induced ellipticity results in a non-zero polarization component along the axis of the second polarizer proportional to the degree of ellipticity. This configuration is sometimes referred to as a plane polariscope.[16] Highly sensitive photoelastic force transducers based on this effect have been made using photoelastic crystals such as quartz.[17] Several types of plastics also exhibit the photoelastic effect, including Polystyrene and
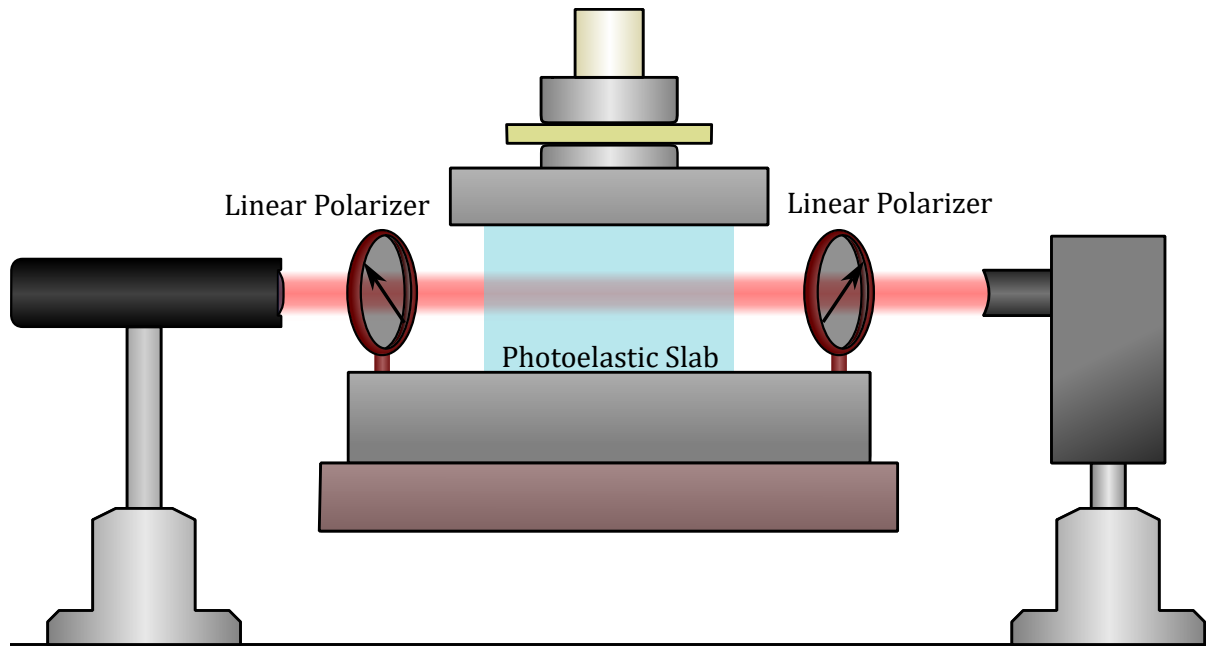
Figure 3.4: Simplified depiction of the photoelastic force sensor.

Acrylic (PMMA).[18] We are now ready to discuss the design of the force sensor used in the quasistatic setup. An illustration of the force detector can be seen in Figure 3.4. The detection system is based on the plane polariscope described previously. As such it consists of a pair of crossed linear polarizers on either side of a rectangular photoelastic slab. A 635nm diode laser is used as the input and a homemade amplified photodetector is used to detect the changes in intensity. The photoelastic slab is made of cast acrylic which has been machined to size and subsequently polished on the ends. It is mounted using a set of machined aluminium clamps. The top clamp serves as the base of the bottom contact probe and the bottom clamp is seated in a machined track, allowing for left to right alignment of the top and bottom contact probe. This assembly is mounted on a baseplate on which the polarizers are also mounted. The baseplate can be shifted back and forth on the stage allowing centring of the top and bottom contacts.

In practice, the laser and photodetector are mounted away from the stage and the light is guided through a series of mirrors. This also simplifies the process of aligning the laser to the acrylic slab.

Optical components were aligned such that the photodetectors maximum peak to peak voltage was measured under an AC load.

3.3.3   Calibration of the Force Sensor

Two calibration procedures for the force sensor were used. In both cases, the sensor is calibrated relative to the reference load cell mounted in the force head. To understand the necessity of two calibration modalities, we must consider the possible ways force can be applied during measurement. Assuming that the acrylic slab is not perfectly homogeneous, we should expect a difference in calibration depending on the position of the stage. This leads to two distinct situations during measurement.

Local Calibration

In the first case, the position of the stage, and hence the DC preload, is fixed throughout a sequence of measurements. Here, the calibration was done by using the piezoelectric actuator, normally responsible for AC loading, to apply an additional DC force component. This made it possible to measure the response of the force sensor over the entire force range of the actual actuator, all while the sample was mounted. The obvious benefit of this approach is that the relative position of the optics remain unchanged during calibration and until measurement has completed. Hence, additional errors due to different positioning of the stage before and after sample mounting are eliminated. This calibration procedure is also easy to automate, making it practically possible to recalibrate between subsections of a larger measurement procedures. An example of a local calibration dataset and its associated fit is shown in Figure 3.5. The fit indicates that it is reasonable to expect a linear response of the force sensor within the range of the AC load. Also note that the output voltage of the photodetector decreases for increasing levels of force.

Global Calibration

In the second case, the movable stage is moved for each calibration point. This is done since the effect of the applied preload is also of interest when characterizing piezoelectric samples. The necessary translation introduces errors associated with the alignment of the photoelastic media. Therefore, meaningful calibrations must in this case be done over the range of translation of the stage. Regions of nonhomogeneity in the acrylic slab could result in random data points significantly deviating from the expected linear behaviour. An example of a global calibration dataset and associated linear fit can be seen in Figure 3.6. As with the local calibration modality, the base assumption of linearity over the force range is justified.
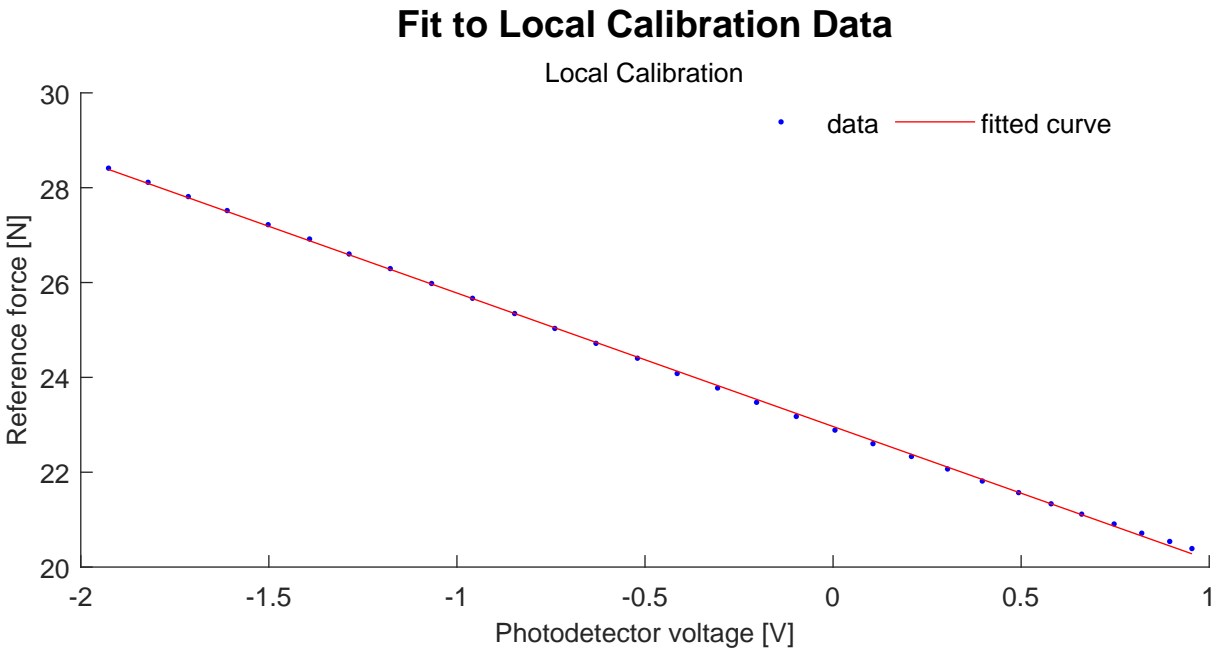
Figure 3.5: Plot of local calibration data and the associated linear fit. *Note: The negative photodetector voltage is a result of a voltage offset in the amplification circuitry.*

Figure 3.6: Plot of global calibration data and the associated linear fit. *Note: The negative photodetector voltage is a result of a voltage offset in the amplification circuitry.*
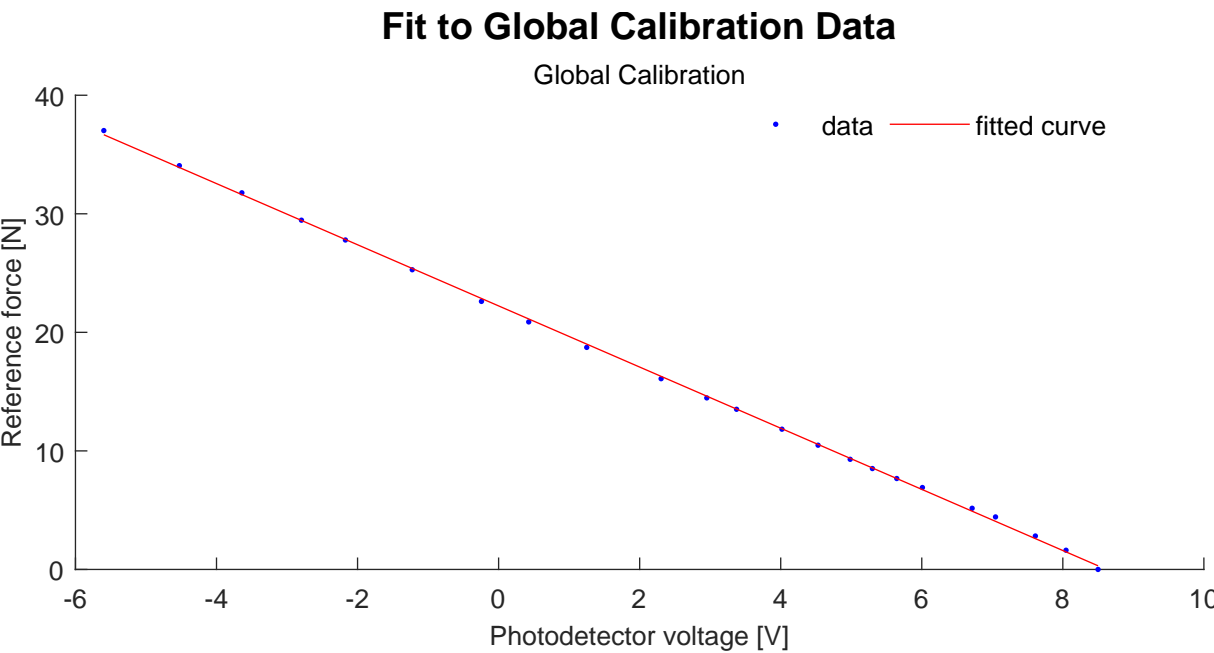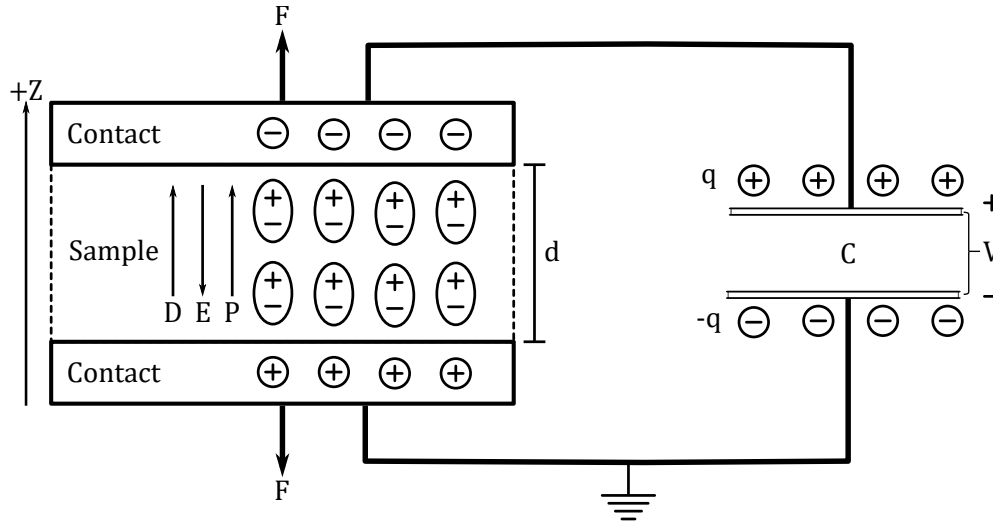
Figure 3.7: Charge measurement using a shunt capacitor assuming sufficiently large capacitance on the shunt capacitor. Free charges on the contacts oppose the electric field due to polarization inside the sample. This is equivalent to short circuit conditions.

3.4   Charge Measurement

As mentioned in Section 2.6.1, measurements must be done under short circuit conditions. Two major approaches are common for achieving this. The simplest approach, is to connect a large shunt capacitor across the piezoelectric sample. An illustration of a charge measurement using a shunt capacitor can be seen in Figure 3.7. The addition of a large shunt capacitor provides a source of free charges, which effectively cancels the electric field across the sample. The charge of the sample can then be calculated from the voltage across the shunt capacitor using[8]

$$C = Q/V \Rightarrow Q = VC. \tag{3.4}$$

Here, the immediate trade-off is that to successfully approximate the short-circuit conditions, a large capacitor is needed. However, the output voltage is inversely proportional to the capacitance. Attempts at measuring charge with a shunt capacitor resulted in poor signal-to-noise ratios. Additionally, there is no compensation mechanism for the impact of cable capacitance, leading to additional uncertainty in the measurement. The natural extension of this concept is to include active components that serve as additional sources of free charge while allowing for the use of smaller capacitances. This is typically done using a charge amplifier.
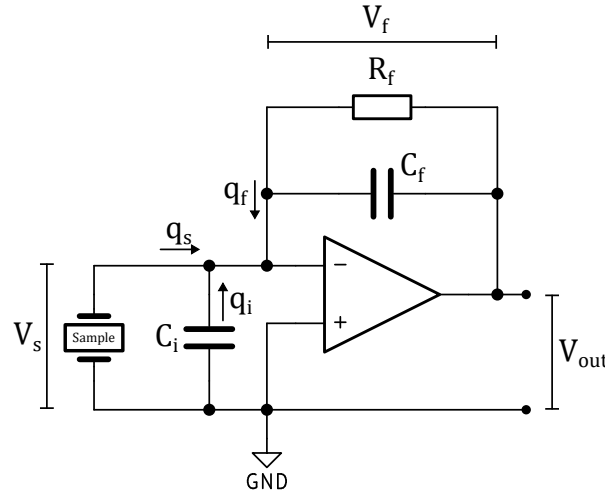
Figure 3.8: Schematic of an ideal charge amplifier along with the associated potentials and charges.

Charge Amplification

The measurement of charge using a charge amplifier is based on the properties of an ideal op-amp. Namely, an ideal op-amp is assumed to have infinite gain and that no current flows through the inputs of the amplifier.[19] Consider the simplified diagram of a charge amplifier which can be seen in Figure 3.8. The op-amp is configured in the inverting configuration, hence the relation between the input potential V_s and output potential V_{out} is given by[20]

$$V_{out} = -G_{int} V_s,$$
(3.5)

where G_{int} is the amplifier gain. The potential difference across the feedback capacitor C_f is then

$$V_f = V_{out} - V_s = V_{out} - \frac{V_{out}}{-G_{int}} = \left(1 + \frac{1}{G_{int}}\right) V_{out}.$$
(3.6)

Applying Kirchhoff's current law in the node of the inverting input yields

$$q_s + q_i + q_f = 0,$$
(3.7)

where q_s is the charge generated on the sample, q_i is the stray charge due to the input capacitance of the cables and connectors and q_f is the charge originating from the feedback capacitor. The right side of the equation is zero due to the assumption that no current flows through the op-amps input. Using $q = CV$ and equation (3.6) we can write

$$q_s = -\left(1 + \frac{1}{G_{int}}\right) V_{out} C_f - \frac{1}{G_{int}} C_i V_{out}.$$
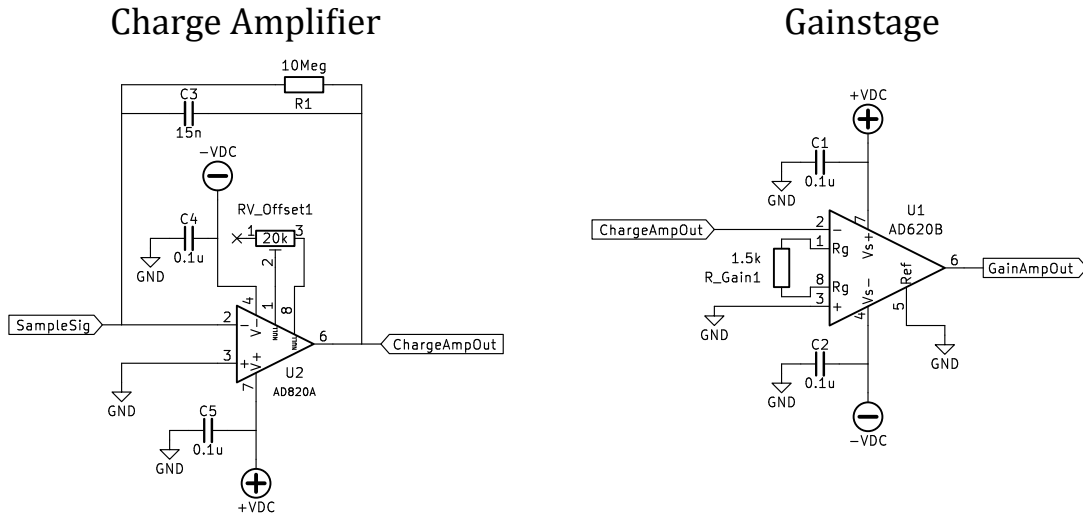(3.8)

Charge Amplifier

Gainstage

Figure 3.9: Schematic of the real charge amplifier.

Evaluating in the limit of infinite internal gain yields the relationship

$$q_s = -V_{out}C_f. \tag{3.9}$$

Hence, the output of a charge amplifier is only proportional to the charge from the sample, and effects of cable capacitance are eliminated. Additionally, when assuming infinite gain, the amplifier will perfectly balance the potential across its inputs, leading to the sample being under short circuit conditions.

Lastly, the feedback resistor R_f is included to allow for discharging the feedback capacitor. This allows measurements of a quasistatic charge signal. The low frequency cut-off is given by:[20]

$$f_l = 1/2\pi R_f C_f. \tag{3.10}$$

A schematic of the design of the charge amplifier built to measure the charge of the setup is presented in Figure 3.9. The amplifier has a charge amplifier stage in the input and a separate gain stage based on a low noise instrumentation amplifier.

The main source of measurement uncertainty in the charge amplifier is the tolerance of the feedback components in the charge amplifier as well as the gain setting resistor of the instrumentation amplifier.

Chapter 4

Benchmarking of the Setup Using Samples of Bulk Lithium Niobate

We are now ready to begin the process of evaluating the accuracy of the resultant meter. For this purpose, samples of Lithium Niobate have been used as a means of comparison.

4.1 Lithium Niobate

I will now briefly describe the structure and relevant material properties of Lithium Niobate. Lithium Niobate ($LiNbO_3$) is a synthetic crystalline material which has found diverse uses in photonics because of its advantageous combination of optical properties. Lithium Niobate exhibits large nonlinear optical coefficients and is also highly electro-optic.[21] Of special interest for the purposes of this report is the piezoelectric properties of Lithium Niobate.

Lithium Niobate is part of the trigonal crystal system, and is a part of the $3m$ point group. It can be thought of as consisting of a series of stacked planar sheets of oxygen in $a_1 a_2$-plane. They are arranged in an imperfect hexagonal close-packed configuration. Lithium and Niobium are arranged cyclically along the c-axis, each taking up one third of the interstitial sites leaving the remaining third of interstices empty. This leads to the formation of dipoles under deformation. This configuration leads to 3 mirror planes oriented perpendicularly to the c-axis. They are oriented with a 120° spacing. [10]

Based on its hexagonal unit cell and according to the standards in [8] the crystallographic axes a_1,a_2,a_3 and c map to a Cartesian coordinate system in the following manner. The Z-axis is chosen such that it is parallel to the c-axis. The positive sense +Z of the Z-axis is determined such that the d_{33} piezoelectric coefficient is positive according to the sign convention described in Section 2.4. The X-axis is chosen to coincide with any one of

	d_{15}	d_{22}	d_{31}	d_{33}
	69.2	20.8	−0.85	6.00
(1) [pC/N]	68	21	−1	6
	74	21	−0.87	1.6
(2) [pC/N]	69.2	20.8	-0.85	6.0

Table 4.1: The piezoelectric coefficients of **lithium niobate**.
(1): As presented in [10], and referenced to by the manufacturer of the Z-cut wafer used for some samples. 3 values are listed for each coefficient, corresponding to values measured by different laboratories.
(2): As stated in the datasheet [22], obtained from the supplier of the X-cut wafer used for some lithium niobate samples.

the a_i-axis. Lastly, the Y-axis is chosen such that it is orthogonal to the Z- and X-axis. The positive sense +Y is found such that d_22 is positive. Lastly, +X is determined such that the X-, Y- and Z-axis, form a right-handed coordinate system. The piezoelectric tensor $\overset{\rightleftharpoons}{d}$, as defined in equation (2.24) of a trigonal 3*m* crystal is given by

$$
\overset{\rightleftharpoons}{d}_{3m} = \begin{bmatrix} 0 & 0 & 0 & 0 & d_{14} & d_{16} \\ d_{21} & d_{22} & 0 & d_{24} & 0 & 0 \\ d_{31} & d_{32} & d_{33} & 0 & 0 & 0 \end{bmatrix} = \begin{bmatrix} 0 & 0 & 0 & 0 & d_{15} & -2d_{22} \\ -d_{22} & d_{22} & 0 & d_{15} & 0 & 0 \\ d_{31} & d_{31} & d_{33} & 0 & 0 & 0 \end{bmatrix}, \quad (4.1)
$$

such that the piezoelectric coefficients of LiNbO$_3$ can be expressed by 4 independent coefficients d_{15}, d_{22}, d_{31} and d_{33}. The piezoelectric coefficients of lithium niobate can be found in Table 4.1.

Lithium Niobate Samples

The lithium niobate samples used as a benchmark came from two differently oriented lithium niobate wafers. Namely, a Z-cut wafer and a X-Cut wafer.

The Z-cut wafer had a thickness of 0.5 mm, and was only polished on the +Z face. The wafer was divided into smaller samples using a diamond saw. Four separate samples obtained from this have been measured using the setup. An overview and description of the samples can be seen in Table 4.2. The names listed in the name column will be used together with the material type to identify the relevant samples when presenting the data. It will also be visible in subtitles of the plots presenting the data from individual measurements. An additional sample was obtained after "Lithium niobate Z-Cut (No.1)" shattered in the process of removing it from the setup. This was included as a separate measurement due to its drastically different size.

Samples from the Z-Cut Wafer

Name	Approximate Size	Geometry	*Note*
Z-Cut (No. 1)	10×10 mm	Square	*Shattered after measurement*
Z-Cut (No. 2)	10×5 mm	Irregular	*From edge of wafer*
Z-Cut (No. 3)	5×5 mm	Irregular	*From edge of wafer*
Z-Cut (No. 4)	10×10 mm	Square	

Table 4.2: Overview of the lithium niobate samples originating from the Z-cut wafer.

Samples from the X-Cut Wafer

Name	Geometry	*Note*
Z-Cut (crosssawn)	Beam	*Too long, parallel edges*
Lithium niobate X-Cut (Asymmetrical)	Irregular Flat	*Shattered flat piece*

Table 4.3: Overview of the lithium niobate samples originating from the X-cut wafer

Several samples were also made from the X-cut wafer. It is only polished on the top +X face. Consider the piezoelectric coefficients listed in Table 4.1. It is clear that under a normal loading measurement, the expected result will be a zero reading. Hence, the wafer was sawn into small beams with different orientations. These were then used as a gauge of the ability to measure coefficients in different directions. Samples prepared in this way have the designation "(crosssawn)" added to their name. The samples originating from the X-cut waver are listed in Table 4.3

4.2 Initial Results and Data Processing

Before delving into the process of understanding the behaviour of the setup, I will start by presenting the result of the first measurement of a reference Z-cut LiNbO3 sample recorded on the system. A plot of the measured piezoelectric coefficient vs. the frequency of the AC load can be seen in Figure 4.1 Comparing the measured d_{33} of Lithium niobate Z-Cut (No.1) to the values d_{33} listed in Table 4.1, the measurement shows reasonable agreement
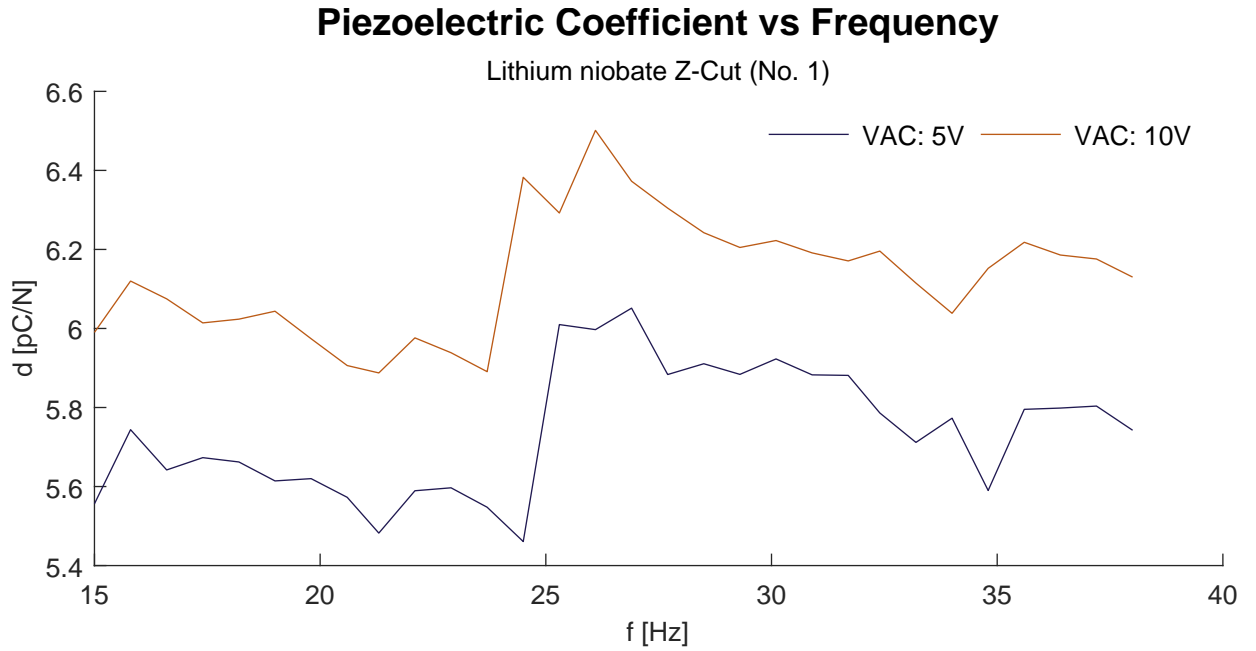
Figure 4.1: *Lithium niobate Z-Cut (No.1), Measurement 1* Plot of the piezoelectric d_{33} coefficient vs. the excitation frequency. Measured at different driving amplitudes.

with the expected values. We should, however, temper our expectations of the reliability of this reading. Looking closer, there is a sudden shift in the recorded value of d_{33} at around 25Hz. This apparently happens regardless of the driving amplitude, and is seemingly frequency dependant. One would not expect such a sharp change in the behaviour of the sample, indicating that it is an effect of the instrumentation.

There are 4 parameters directly impacting the way in which the sample is excited. These are the frequency (f), the driving amplitude (VAC), the driving offset (VDC) and the static preload (FDC). The frequency and preload require no further explanation. The driving amplitude and driving offset are the input parameters of the signal generator controlling the piezoelectric actuator. VAC is therefore proportional to the magnitude of the AC force. Specifically it is the peak to peak amplitude of the sinusoidal signal used to control the actuators dedicated driving electronics. Equivalently, VDC represents the DC voltage offset of the control signal. In practice the driving circuit used in the setup cannot supply negative voltage to the actuator. Therefore, it is necessary to offset the control signal by at least half of VAC. To avoid having to adjust VDC every time a change was made to VAC, it was set to a default value of 5V. This does, however, have the effect of adding an additional contribution to the preload. This contribution is not included in the associated reading of the DC force measured by the reference load cell. Equivalently, the quantity FDC should be understood as the preload when the actuator is turned off.

We can try to glean some insight into the artefact by considering the way a measurement was done. Measurements made on the setup were done using a set of measurement routines, defining the parameters of each data point.

The dataset presented in Figure 4.1 was measured using a measurement routine that was intended as a means of quickly gauging the magnitude of a sample's piezoelectric coefficient. As such, it is of a relatively small resolution and includes no repeated measurements at a single set of parameters. It will, however, serve as a reasonable means of illustrating the order of operations during measurements. The measurement routine sweeps through a preset frequency range, recording data points at different levels of *VAC* at each point in the sweep. Consider the plot of the piezoelectric coefficient, which can be seen in Figure 4.2. Here, data points are arranged in the order they were recorded. The bottom plot indicates the state of the measurement parameters *f* and *VAC* at each data point. It should be read such that a parameter value of 0 corresponds to the minimum value listed in the legend and such that a parameter value of 1 corresponds to the maximum value of the parameter listed in the legend. Although cumbersome as a means of representing the dependence of frequency and driving amplitude, it provides a way of determining the nature of the artefact. It can be clearly seen that the shift occurs only once during the entire measurement and persists for the remaining data points. Hence, this shift is not necessarily directly related to the transition in frequency such as the representation in Figure 4.1 could otherwise imply. Without removing the sample, the setup was recalibrated locally (See Section 3.3.3) and the measurement was redone in the range where the artefact had previously occurred. The result of this can be seen in Figure 4.3. This time, no artefact was present. This suggests that the artefact was due to a randomly occurring shift in the positioning of a setup component or in the mounting of the sample.

4.2.1 Data Processing

We will now go through how the piezoelectric coefficient was calculated on the basis of the data acquired during measurements. The raw waveforms of a single data point in "LiNbO$_3$ Z-Cut (No 1) Measurement 1" is shown in Figure 4.4 First, notice the massive improvement in signal-to-noise ratio when comparing photodetector output to the output of the strain gauge based force sensor shown in Figure 3.3. The high quality of the signal from the photoelastic force sensor negates the need to introduce any filtering or data smoothing steps in the post-processing of the force signal. This is echoed in the signal from the charge amplifier. Hence, the first step of the data processing procedure is simply to convert the voltage signals into their corresponding quantities. The signal of the charge amplifier was converted by dividing the signal with the gain of the gain stage to find the output voltage of the charge amplification stage. This voltage signal is converted to a charge signal by using equation (3.4). Since both the charge amplification stage and
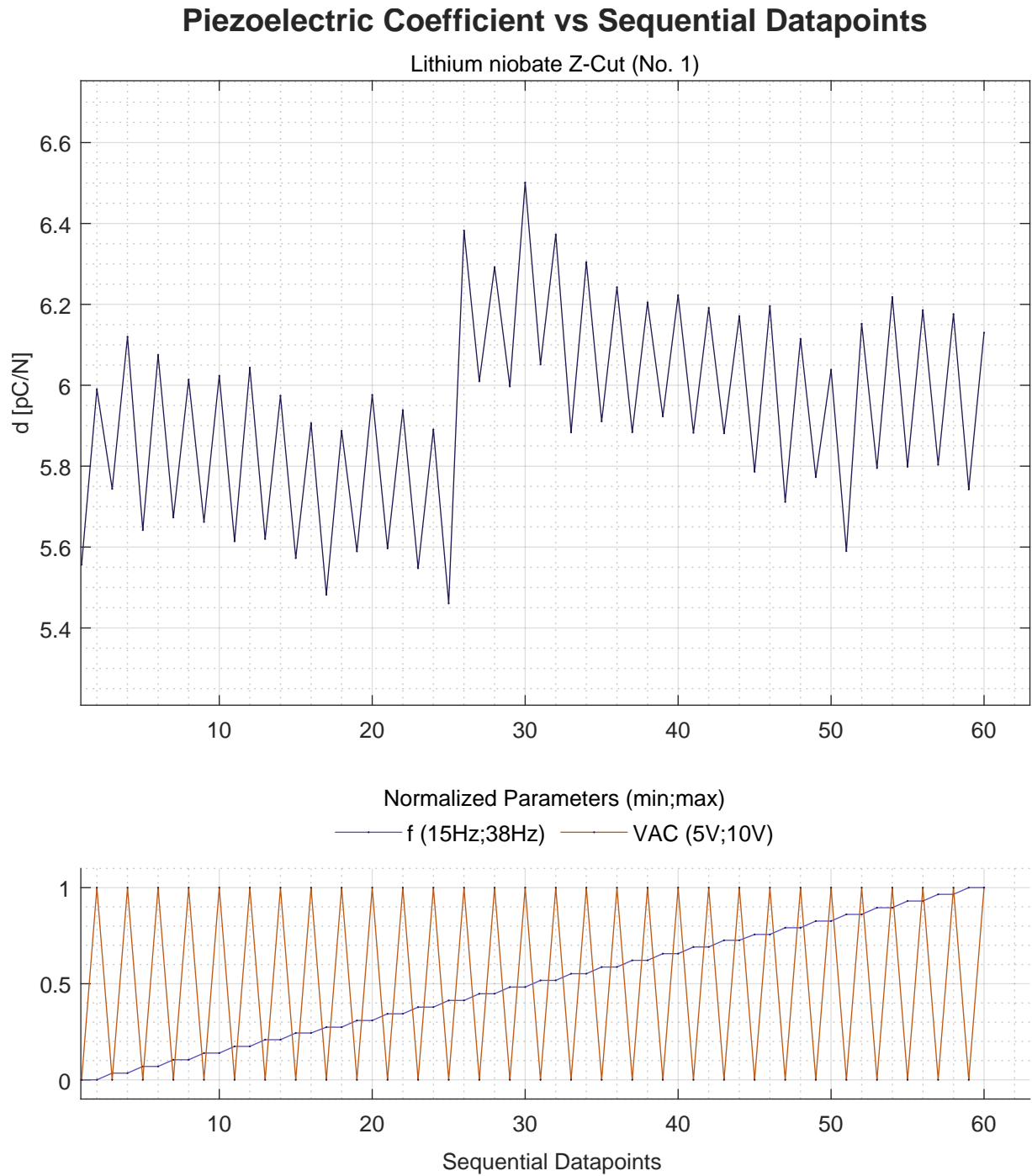
Figure 4.2: *Lithium niobate Z-Cut (No.1)* Plot of the measured piezoelectric d_{33} coefficient. Plotted vs. the n'th data point since start of measurement. The bottom plot illustrates the state of measurement parameters for each data point.
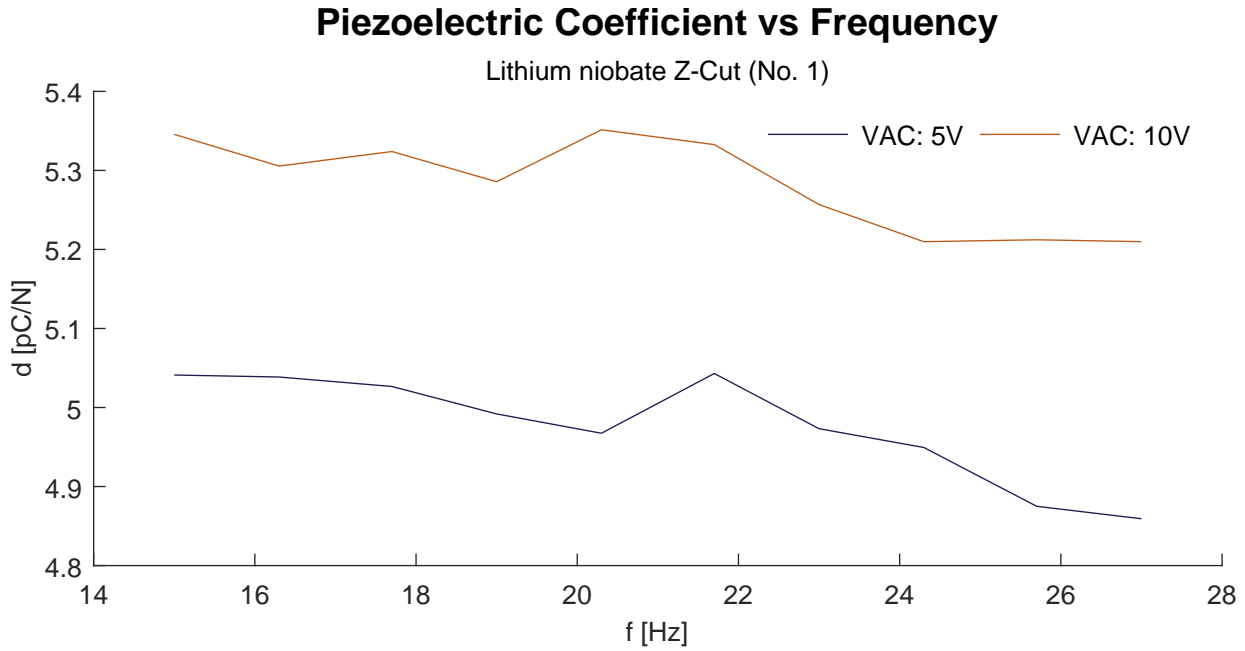
Piezoelectric Coefficient vs Frequency
Lithium niobate Z-Cut (No. 1)

Figure 4.3: *Lithium niobate Z-Cut (No.1), Measurement 2:* Plot of the piezoelectric d_{33} coefficient of vs. the excitation frequency. Measured at different driving amplitudes.

the gain stage are inverting amplifiers, a sign change does not occur during this conversion. The voltage output of the photodetector is converted to a force by using the linear fit found during the calibration procedure. The conversion of the waveform, shown in Figure 4.4, is presented in Figure 4.5. As an additional step, the mean of each signal is evaluated and subtracted from the respective waveform. This is done simply to remove the DC components of the signals. After conversion the piezoelectric coefficient is calculated using equation (2.35). The question of which quantity should be evaluated remains. To evaluate this, a set of simulated signals were generated and a large randomly generated signal noise was added to simulate imperfect measurement conditions. This included a relatively large contribution of 50Hz line noise since this was found to be the dominant source of electrical noise on measurements made on the setup. One approach to comparing the charge and force signals is simply to divide the entire waveform datasets and return the mean of the calculated piezoelectric coefficient as the value of the data point. This approach turned out to be sensitive to line noise contributions and was therefore abandoned. Alternatively, the ratio of the signals root-mean-square values can be evaluated. This approach was abandoned due to sensitivity to any remaining DC components and because it removes the sign information of the measured piezoelectric coefficient. The final approach was based on a digital implementation of lock-in amplification.[23] This consistently returned an accurate amplitude, even if the noise levels of the simulated signals were unrealistically large.
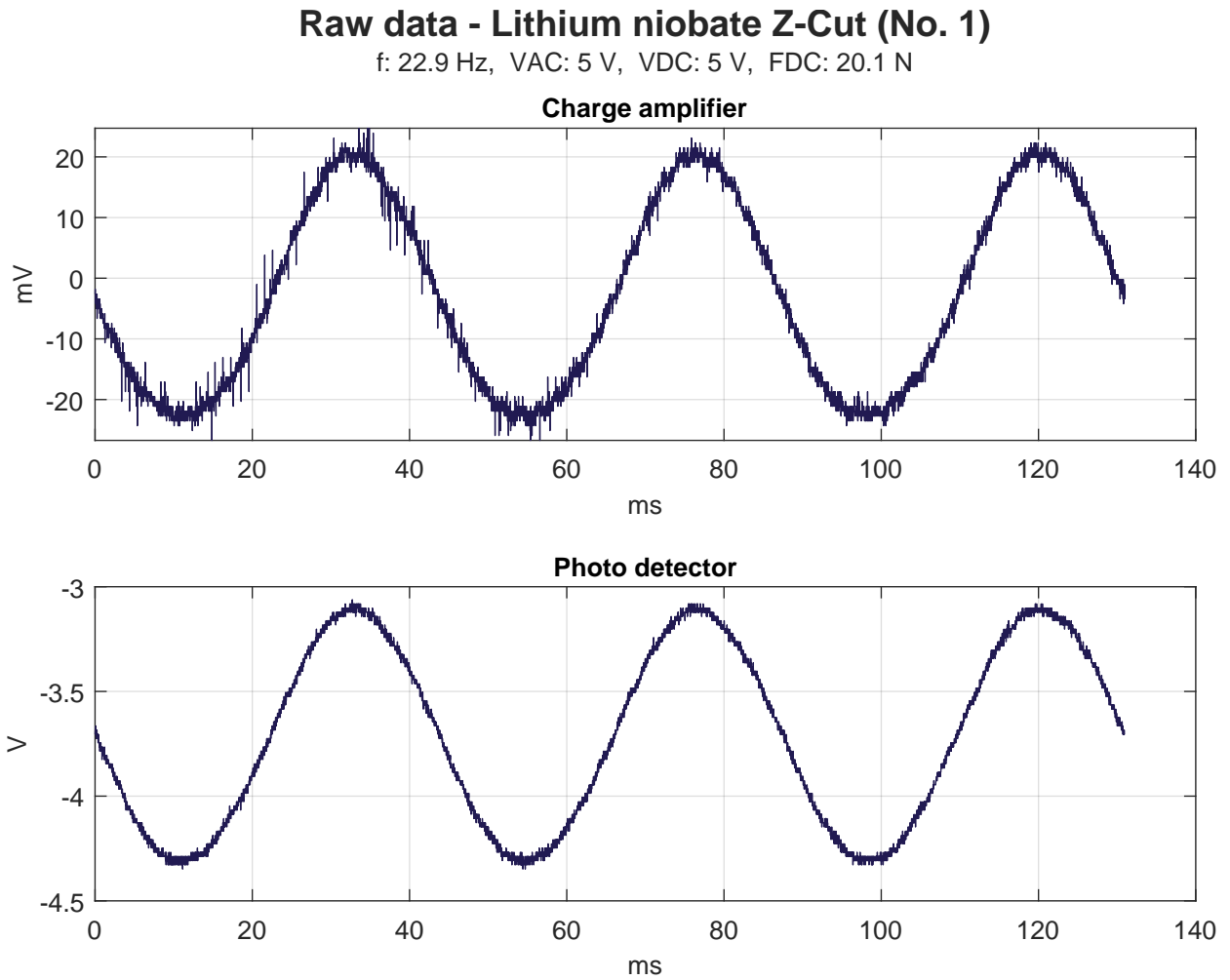
Figure 4.4: *Lithium niobate Z-Cut (No.1) Measurement 1:* Plot of the raw output voltages of the charge amplifier and photodetector, representing a single data point.
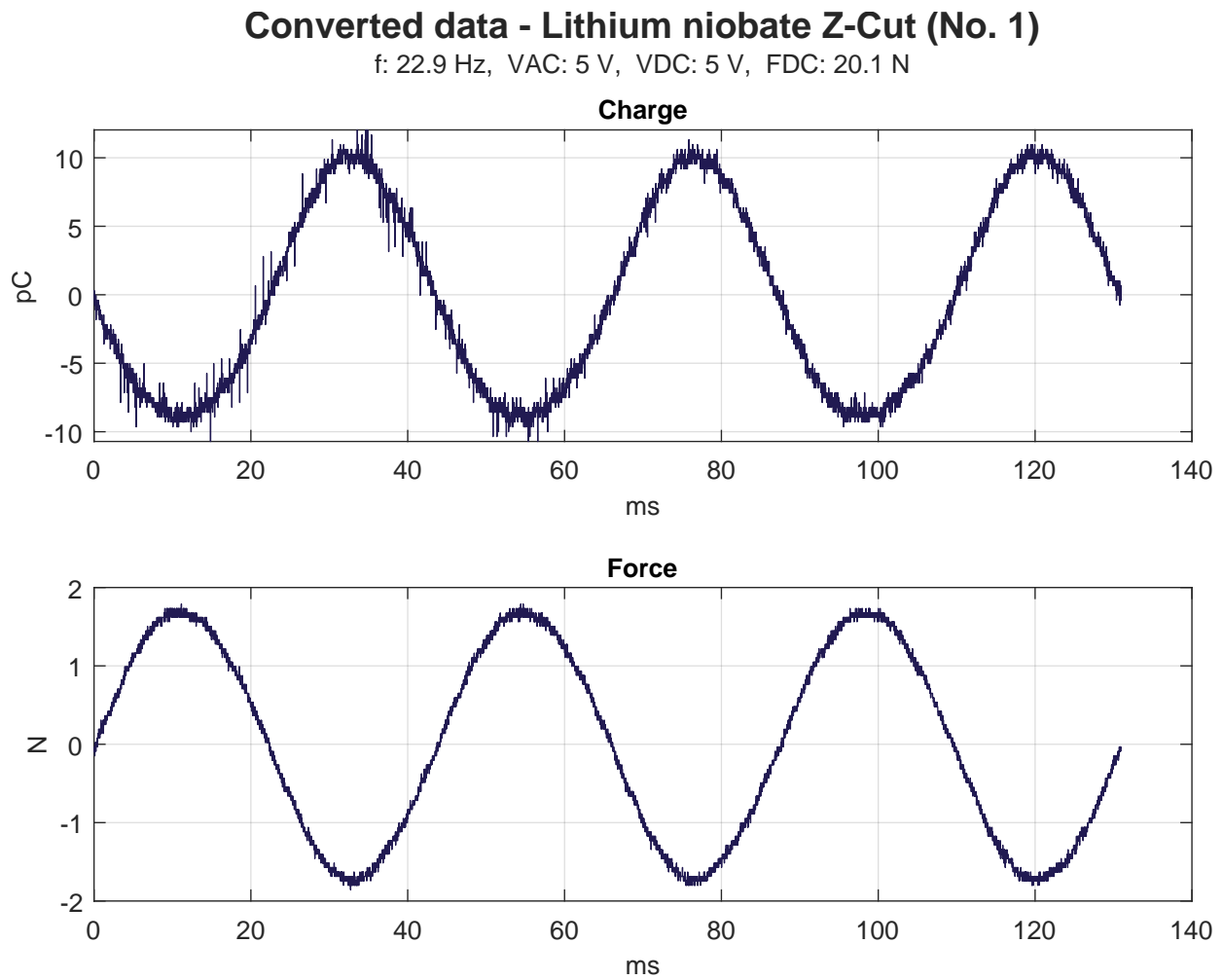
Figure 4.5: *Lithium niobate Z-Cut (No.1), Measurement 1:* Plot of the Charge and Force output of a single data point.

Lock-in detection requires the generation of a reference signal. This reference should be of the same frequency and phase as the input signal. In the implementation used here, a reference signal with amplitude 1 was generated using the driving frequency associated with the data point. The only proviso of this approach is the determination of the phase. The output amplitude is sensitive to the difference in phase, with a dependence going as $A_{out} \propto cos(\phi_s ig - \phi_r ef)$. Conveniently, the triggering system of the oscilloscope has consistently ensured that the phase of the acquired waveforms has remained unchanged across measurements. Under the assumption of conducting measurements quasi-statically, we should not expect a phase delay during measurements. Consequently, the reference phase of the lock-in calculation was set to $0 rad$ throughout all measurements. Measurements conducted such that the sign of the piezoelectric coefficient should be negative, correspond to an apparent pi phase shift of the charge signal. This conveniently means we can use the phase information of the signals to detect the sign of the piezoelectric coefficient.

For the last time, we will remind ourselves of the positive sign convention discussed previously. Remember that a positive d_{33} corresponds to the development of positive charge across the +Z face when the sample is held under tension. Since the Berlincourt type meter applies a compressive stress, the sign must be inverted as the last step.

4.3   The Effects of Measurement Parameters

We will now attempt to describe the observed effects of different measurement parameters. We will start by presenting the result of measurements made at different levels of preload. In general, lithium niobate is considered stable across different frequency ranges. A dependence of the measured d_{33} coefficients on the magnitudes of the DC and AC stresses is well documented in the case of piezoelectric ceramic materials.[24]

4.3.1   Changes of Measured Piezoelectric coefficient over Different Levels of Preload

We will start by looking at the effect of the applied prestress when conducting measurements on lithium niobate samples. The effect of the prestress on the measurement of sample 3 is shown in Figure 4.6. The measurement was conducted by manually tightening the preloading screw in between data points. There is no clear point of stability suggesting an optimal choice. We can, however, look at the associated RMS values of the photodetector and charge amplifier. These are shown in Figure 4.7. This shows that the response of the photodetector is approximately linear until a preload of approximately 20 N is reached. The sample response is linear in the region between 11 and 30 N: Hence, we should aim to preload the samples at a FDC level between 14 N and 18 N
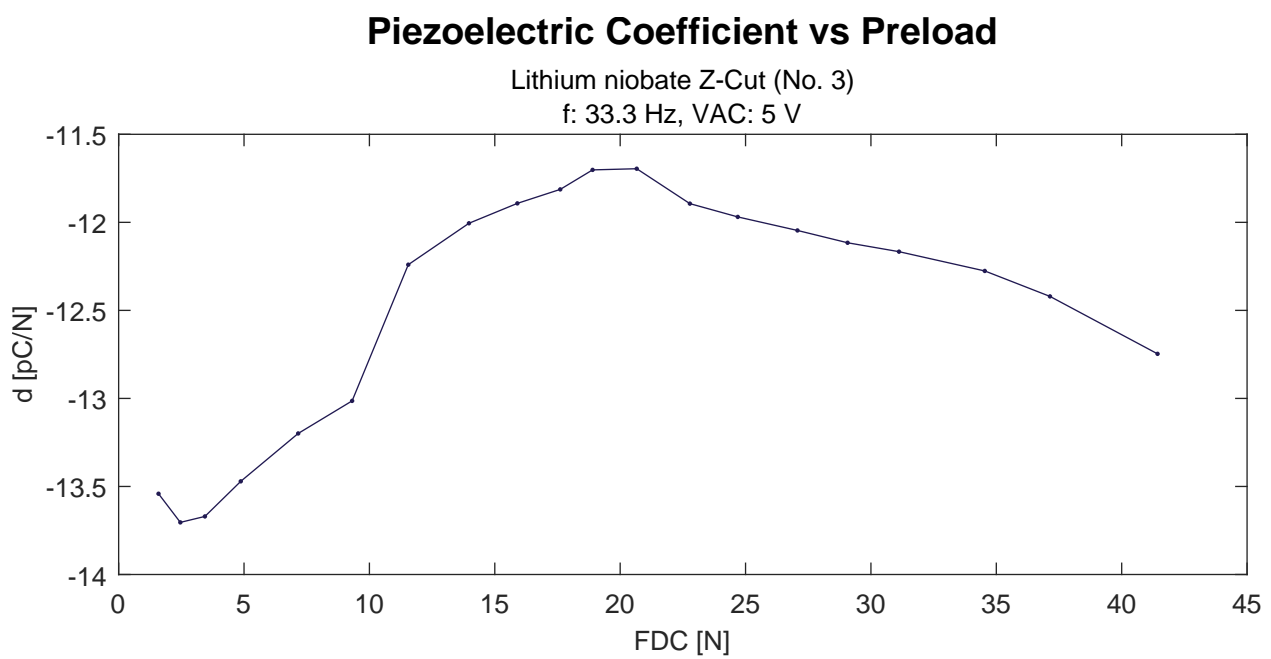
Figure 4.6: *Lithium niobate Z-Cut (No.3):* Plot of the piezoelectric d_{33} coefficient vs. the measurement preload.
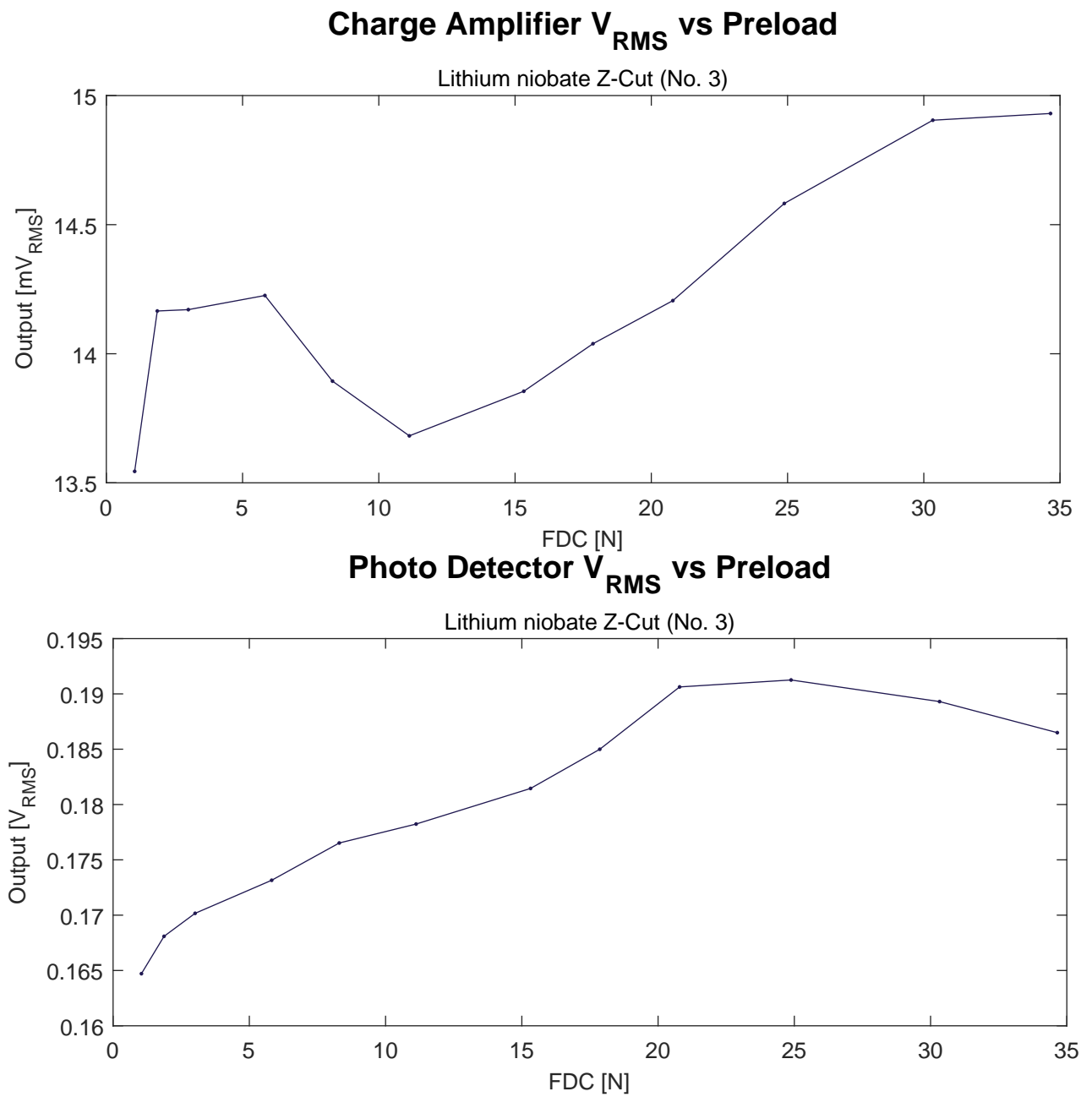
Figure 4.7: *Lithium niobate Z-Cut (No.3):* RMS voltage values of the photodetector and charge amplifier vs. the measurement preload.

4.4 The Dependence on the AC Load

As is the case with the static VAC, the measured d_{33} coefficient shows a dependence on the applied AC forces when measured in a quasistatic meter. The effect of the AC load level for different lithium niobate samples is shown in figures 4.8, 4.9, 4.10 and 4.11. The measurement was made at a single default frequency and the preload level was not changed throughout the measurement. Samples 3 and 4 were mounted with the +Z face pointing in the opposite direction compared to samples 1 and 2. Hence, the measured $d_3 3$ is negative. In all cases the value of the piezoelectric coefficient changes over the range of measurement. Measurements made on samples 2 and 3 show a decrease in d_{33} over the measurement and samples 3 and 4 increases over the same measurement range. This suggests that this is largely a consequence of the instrumentation. The measurement of sample 1 provides two separate amplitude sweeps allowing for comparison of the effect in different ranges. By plotting the measured d_{33} versus the time since the start of measurement, we can clearly see that this change in d_{33} is dominated by a time dependant effect. (See Figure 4.12). However, notice the discrete shift in value in the point immediately after restarting the amplitude sweep using at a different frequency. This artefact is the closest indication of the actual impact of the AC Load. At around 7V the signal generator switches to a higher power output mode. This is audible when standing next to the generator. This change seems to be associated with a shift in the measured d_{33}

4.5 The dependence on the frequency

As was previously mentioned, the d_{33} coefficient of lithium niobate is thought to be stable across the lower frequency ranges. The effect on the driving frequency load level for different lithium niobate samples is shown in figures 4.13, 4.14, 4.15 and 4.16. The measurement was made at a single default driving amplitude, and the preload level was not changed throughout the measurement. Reviewing the result shows a slow, small linear increase in the measured d_{33} coefficient.
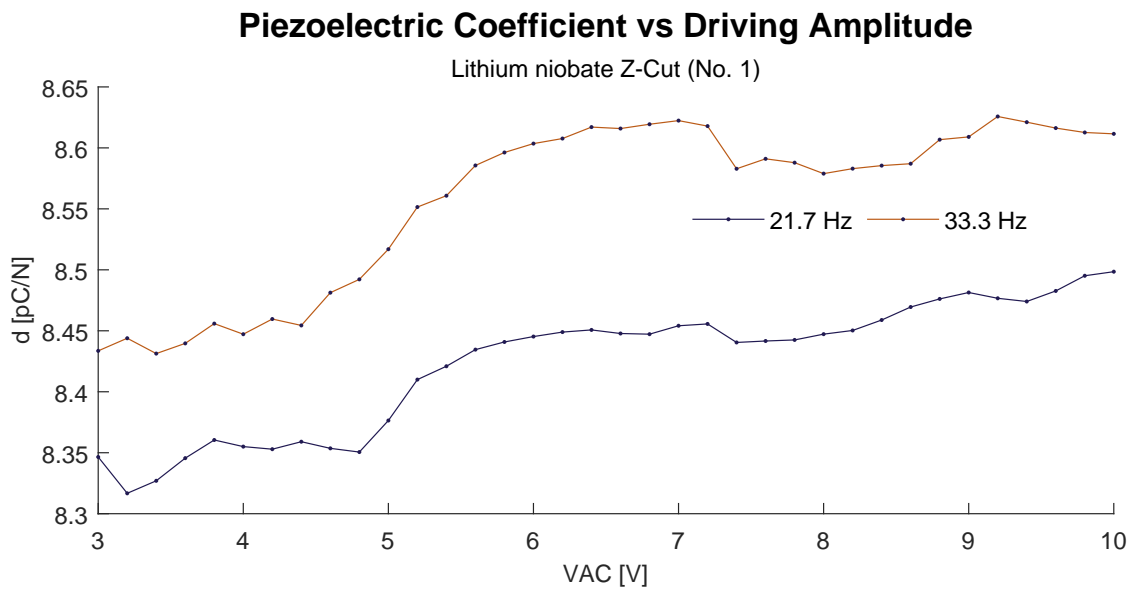
Piezoelectric Coefficient vs Driving Amplitude

Figure 4.8: *Lithium niobate Z-Cut (Piece of No. 1):* Plot of the piezoelectric d_{33} coefficient vs. the measurement VAC.

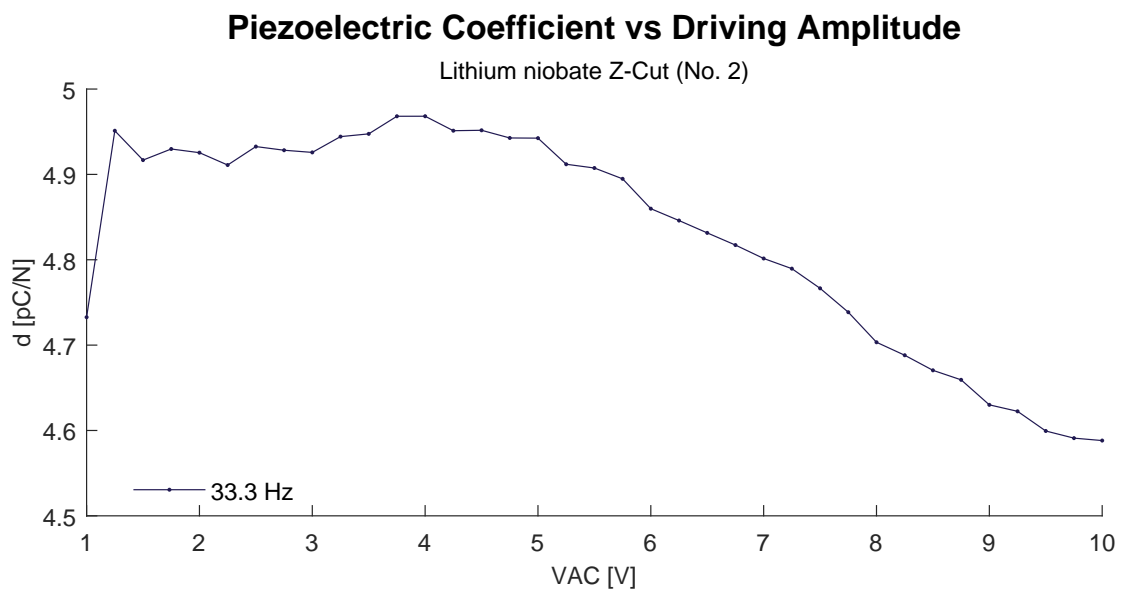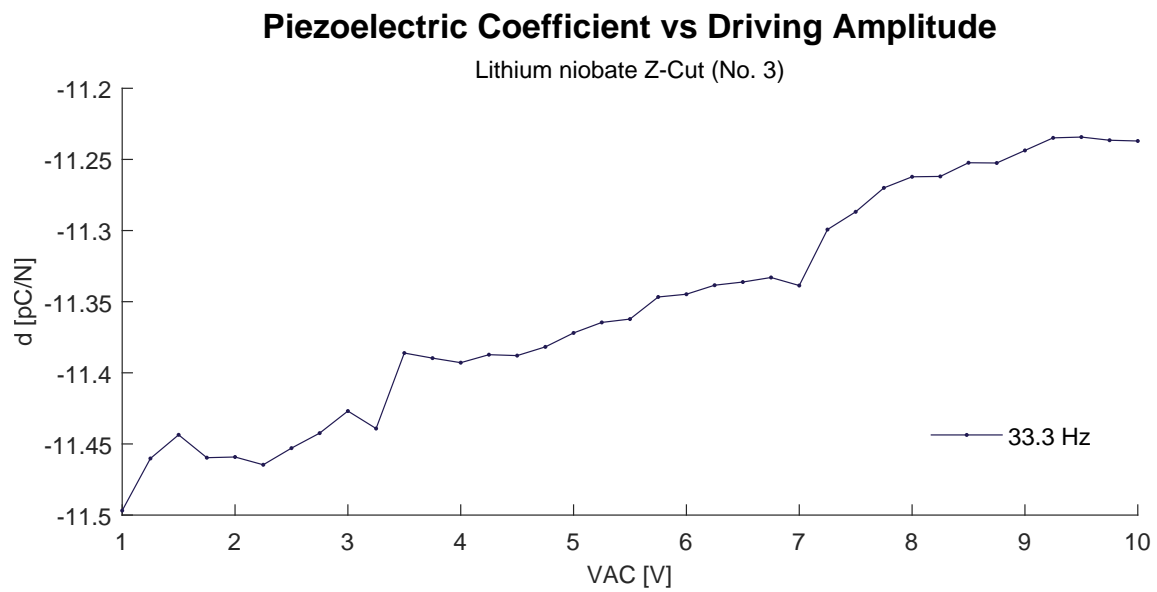## Piezoelectric Coefficient vs Driving Amplitude

Figure 4.9: *Lithium niobate Z-Cut (No.2):* Plot of the piezoelectric d_{33} coefficient vs. the measurement VAC.

Figure 4.10: *Lithium niobate Z-Cut (No.3):* Plot of the piezoelectric d_{33} coefficient vs. the measurement VAC.
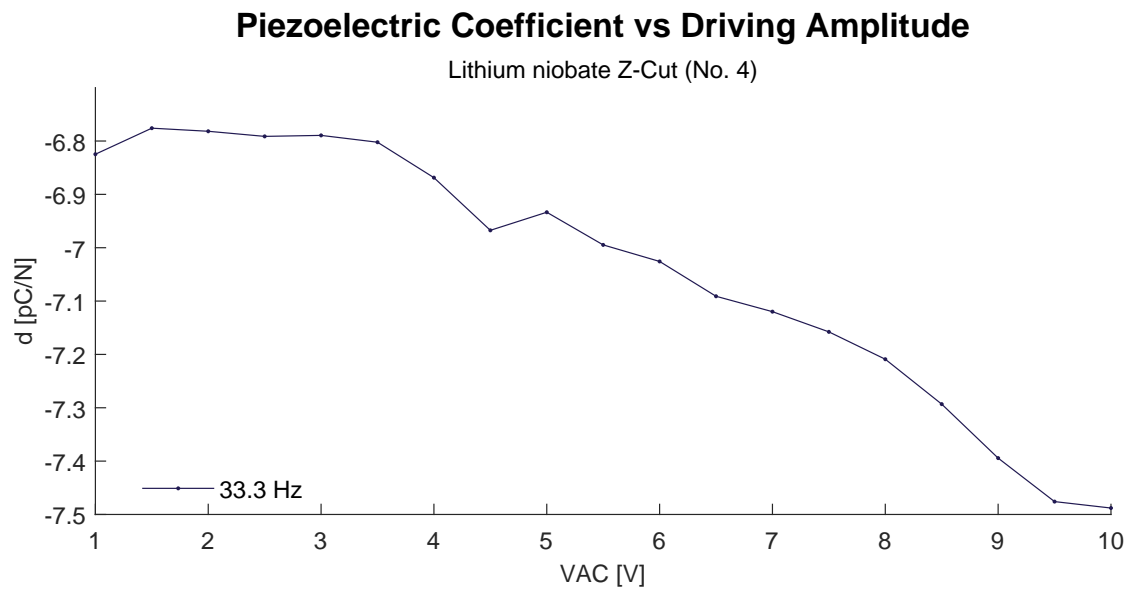

Figure 4.11: *Lithium niobate Z-Cut (No.4):* Plot of the piezoelectric d_{33} coefficient vs. the measurement VAC.
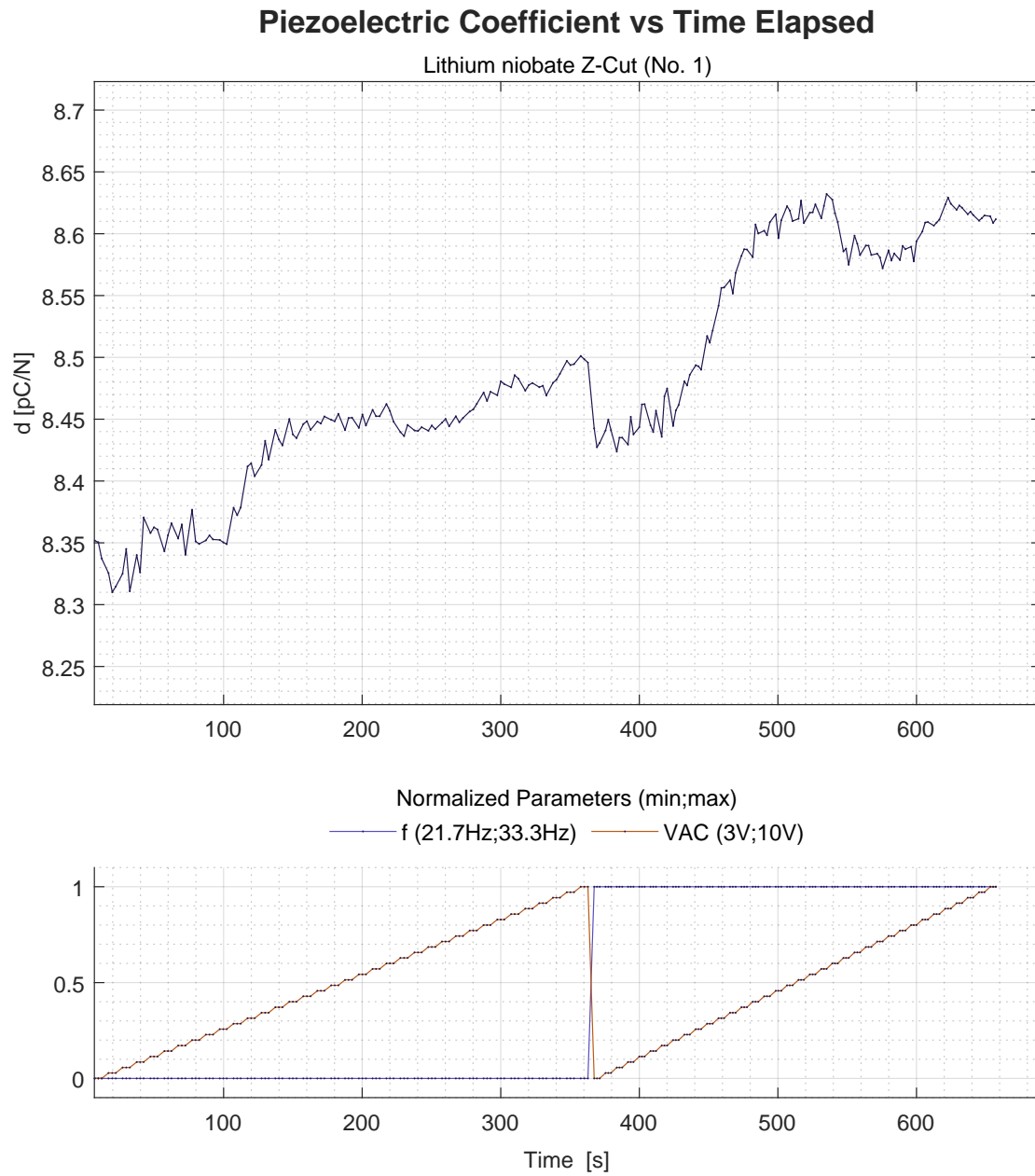
Figure 4.12: *Lithium niobate Z-Cut (Piece of No. 1):* Plot of the piezoelectric d_{33} coefficient vs. time since start of measurement.
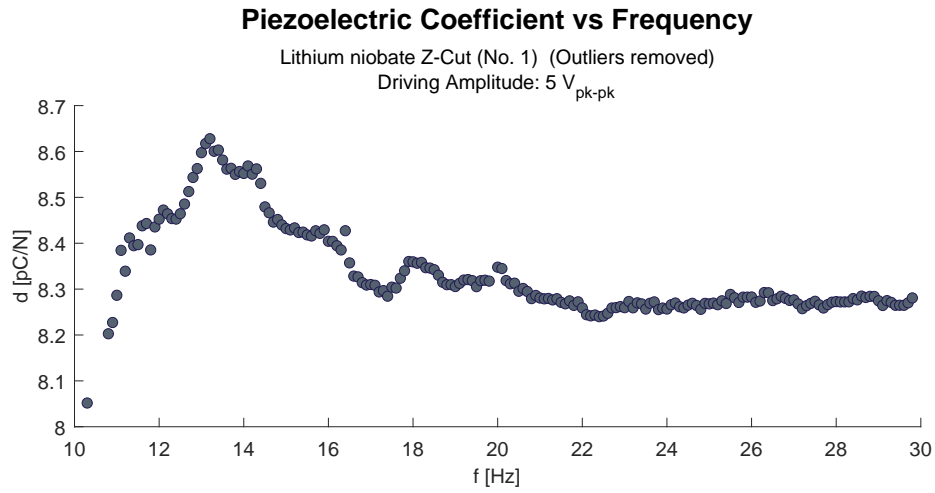
Figure 4.13: *Lithium niobate Z-Cut (No.1):* Plot of the piezoelectric d_{33} coefficient vs the measurement frequency. Isolated large outliers have been removed.
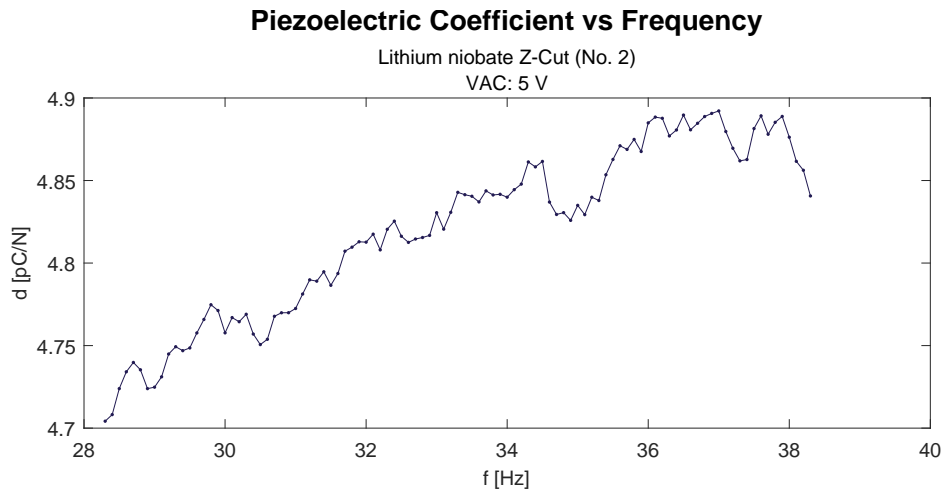

Figure 4.14: *Lithium niobate Z-Cut (No.2):* Plot of the piezoelectric d_{33} coefficient vs the measurement frequency.
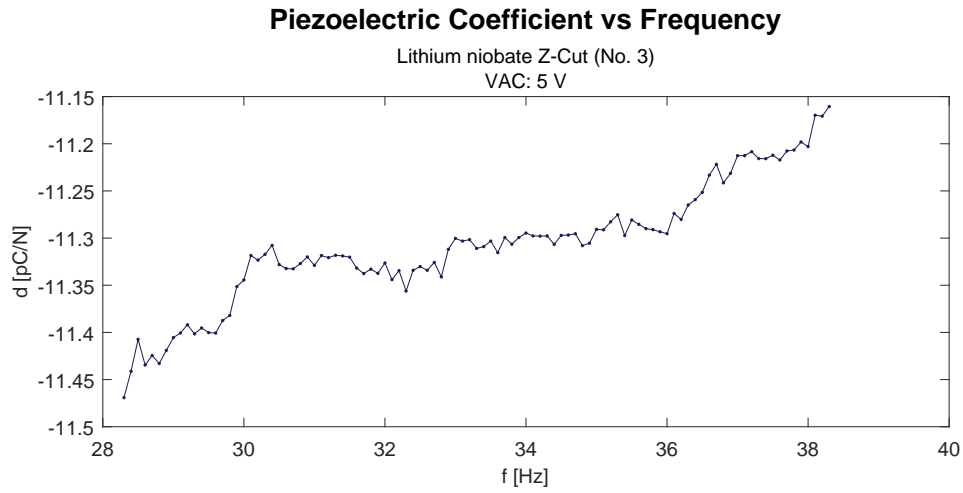
Figure 4.15: *Lithium niobate Z-Cut (No.3):* Plot of the piezoelectric d_{33} coefficient vs the measurement frequency.
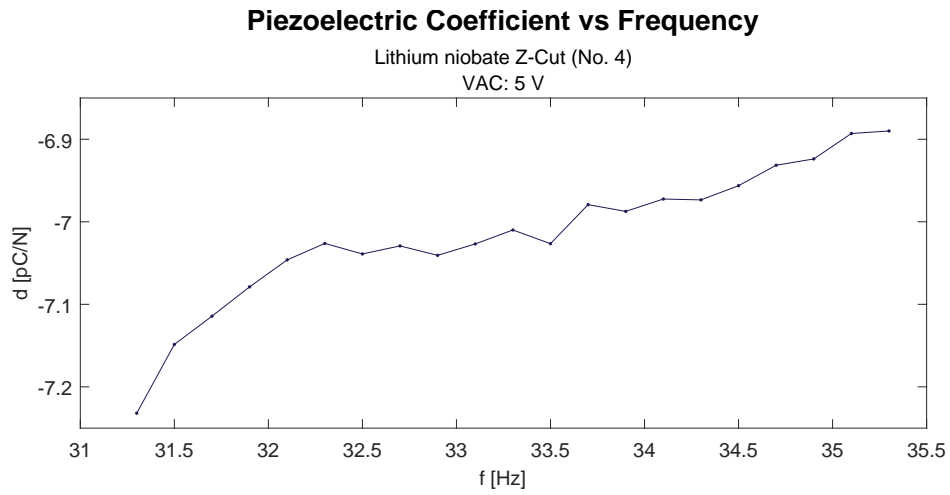

Figure 4.16: *Lithium niobate Z-Cut (Piece of No. 1):* Plot of the piezoelectric d_{33} coefficient vs the measurement frequency.

4.6 Stability of Quasistatic Measurements

Piezoelectric Coefficient vs time since mounting
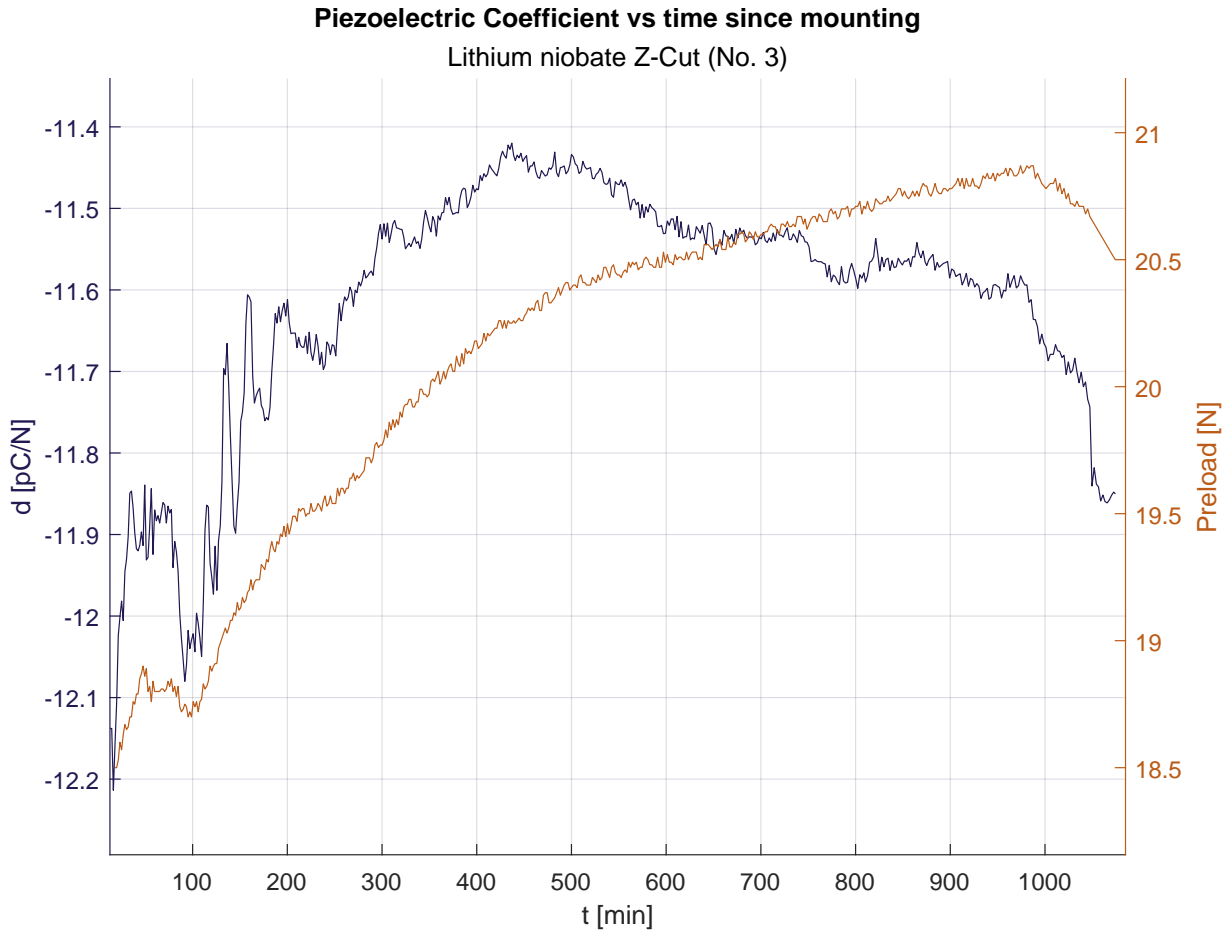Lithium niobate Z-Cut (No. 3)

Figure 4.17: *Lithium niobate Z-Cut (No.3)* Plot of the measured piezoelectric d_{33} coefficient, over a period of several hours. Note, the additional overlay showing the measured preload just before each recording data point was recorded.

We have encountered several cases where the change in the piezoelectric coefficient seems to predominantly be a consequence of the time spent in the setup. Therefore, a series of identical measurements were made using the "Lithium niobate Z-cut (No 3)" sample. The sequence recorded the d_{33} coefficient approximately every two minutes over several hours. Measurement parameters were kept the same throughout the entire measurement. The result can be seen in Figure 4.17 This showed a clear instability over the period of the measurement.

By looking at the overlay showing the measured preload, we can see that it never manages to stabilize. This seems to be the dominant reason that the previous measurements

showed a drift over the elapsed time. We can further subdivide the plot into two regions. In the first region from $0min$ to approximately $450min$ is looks as if the system is going through a stabilization phase. This is evident since the variation in the measured d_{33} between neighbouring data points decreases as time progresses. Simultaneously, the change in slope of the preload decreases. In the second region the slope of the piezoelectric coefficient reverses and the slope of the preload becomes constant, representing a different phase of the system. A possible interpretation is that the sample and photoelastic sensor go through a relaxation phase due to being under load for an extended period of time and that this is what is seen in the first region. A possible reason for the increase in preload is then that vibrations due to the AC force causes a slow creep of the stage lead screw.

Throughout this chapter, we have looked exclusively at Z-cut lithium niobate samples. Disregarding the effect of drift in time and comparing the d_{33} coefficients of the presented data, leads to the following conclusion. Several measurements on the same sample tend to yield equivalent results. However, there is a large variability in the measured coefficient across different samples. Equivalently, reversing the polling direction of the measurement leads to a large offset in the recorded coefficient. A possible explanation for this concerns the fact that only the +Z face of the Z-cut lithium niobate wafer was polished. When examining the setup, one will notice that the quality of the electrical connections to the top contact probe are significantly more fragile than the connections to the bottom negative contact probe. Hence, the offset effect might be a consequence of the difference in resistance. This difference is essentially minimized when the polished side is pointed toward the top contact and maximized in the opposite direction. Hence, d_{33} should be closest to the actual piezoelectric coefficient when polling in the positive direction. This is supported by the data.

4.7   Response of the Samples from the X-cut Wafer

As a sanity check, we will quickly go through the measured piezoelectric coefficients of the lithium niobate samples originating from the X-cut wafer. Consult Table 4.3 for an overview of the samples. Since they were cut from the cross-section of an X-cut wafer, we should expect a certain miss alignment of the sample faces compared to the expected face. In the case of the X-Cut sample (shown in Figure 4.18) we do measure a negative piezoelectric coefficient. We should expect a reading of zero. It can be sufficiently explained by considering the irregular geometry of the sample. This might induce shear strains in the 5 direction, leading to an output. d_{15} is approximately 10 times larger than d_{33}, hence this is an acceptable result. The result of the Z-cut homemade sample can be seen in Figure 4.19. This result shows agreement with measurements made using negative polling of the reference Z-cut samples.

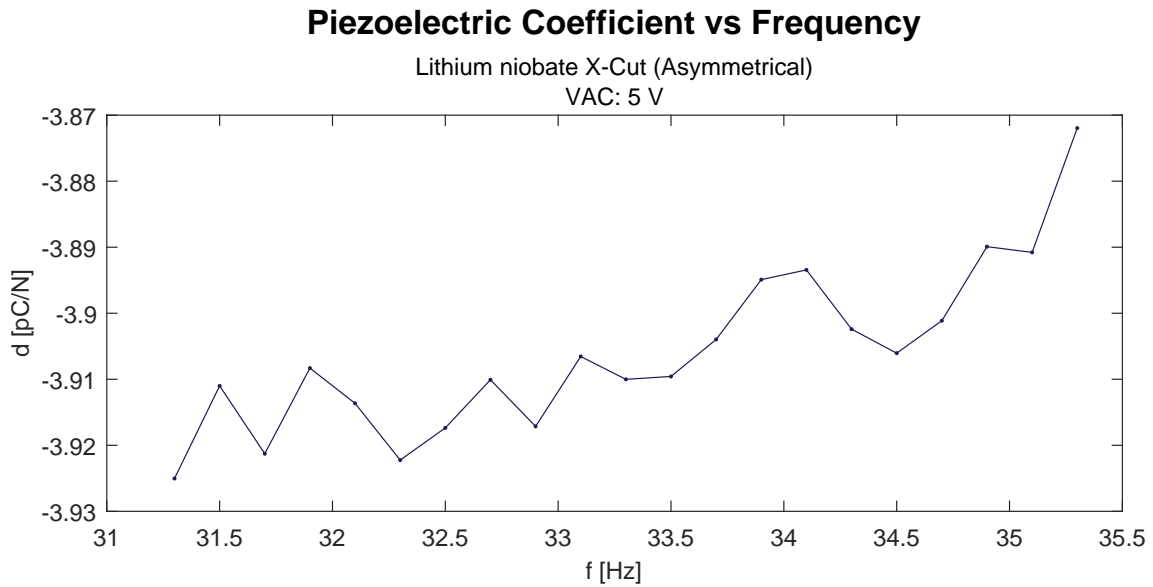**Figure 4.18:** *Lithium niobate X-Cut (Asymmetrical):* Plot of the piezoelectric d_{11} coefficient vs. the driving frequency.
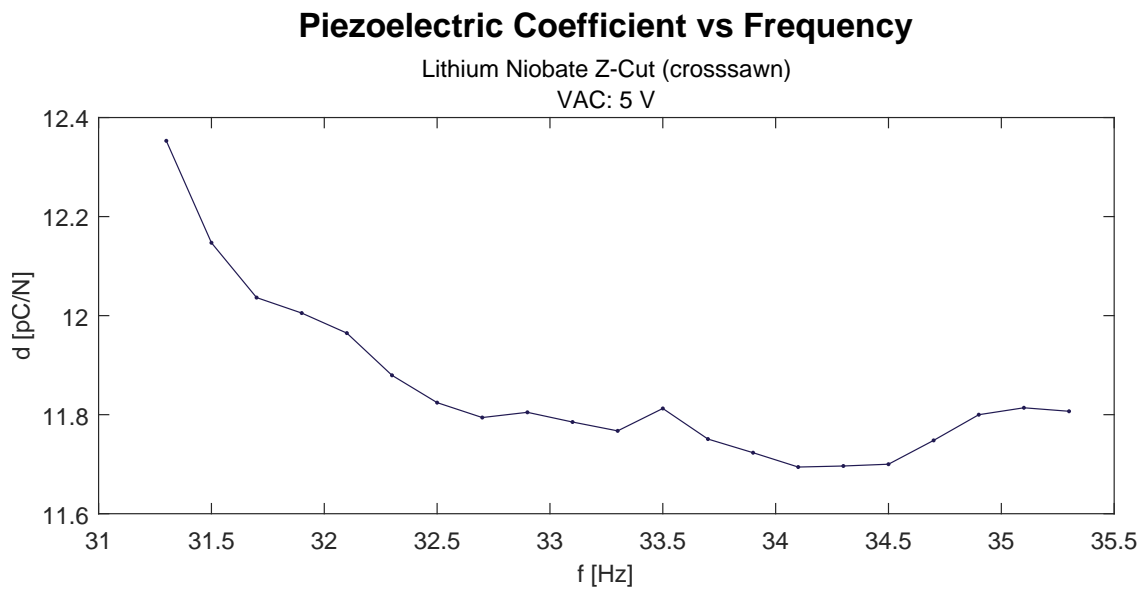

Figure 4.19: *Lithium niobate Z-Cut (crosssawn):* Plot of the piezoelectric d_{33} coefficient vs. the driving frequency.

4.8   Summary of the Benchmarking Process

Based on the presiding chapters, we will now summarize the results and suggest methods of improving repeatability and accuracy of the measurement system. The main issue limiting accuracy and repeatability in the measurement setup is the time-dependant drift seen during all parameter sweep measurements. Secondly, the magnitude of the measured d_33 is substantially different depending on polling direction. This indicates the that the inputs of the charge amplifier behaves asymmetrically.

Another potential source of this behaviour is the generation of charges due to the triboelectric effect, that is, the transfer of surface charges from one material to another when they are rubbed together or repeatedly tapped together. Considering the mounting of the contact probes, they effectively sit between two triboelectric interfaces. The interface between a piece of metal and nylon can generate surface charge densities in the order of $10^-3 C/m^2$.[25]

In addition to the tendency of the measurement preload to increase during measurement, instability of the system may also be affected by relaxation effects in the Acrylic Photoelastic sensor. This is corroborated by the ability to repeat the measurement results of the same sample, when recalibrating between measurements.

Mechanical effects leading to the movement of the stage during measurement must be removed before evaluating the effect of relaxation on the photoelastic sensor. A reasonable first attempt could include installing a locking screw, reducing the ability of the lead screw to auto-adjust.

A certain amount of time drift is inevitable, since the piezoelectric sample itself experiences relaxation under constant loading.[26]

Chapter 5

Conclusion

During the writing of this thesis the basis of piezoelectric measurement has been explored and through many iterations of setup design, the necessary considerations for the design of such a meter have been described. The possibility of using low-cost high availability components to build a Quasistatic d_{33}-meter that measures piezoelectric coefficients without the use of an inline reference samples has been explored and the meter has been fabricated.

A novel approach to force sensing in piezoelectric measurement systems has been developed. Using two linear polarizers, a piece of ordinary cast acrylic was used in an optical force sensor based on its photoelastic properties. This sensing system had an excellent signal-to-noise ratio and was sufficient in providing dynamic force readings in the frequency range of the setup.

A charge amplifier has been built using common electronic components available at any electronics supplier and it has been shown to feature reasonable signal-to-noise levels, as well as being able to handle the low frequencies inherent to quasistatic measurement.

Measurement were consistently accurate within $\pm 7 \text{pC/N}$

The resultant experimental setup did, however, suffer from issues related to measurement drift over time. Exceeding the levels expected due to the relaxation of the sample itself. Additional investigation is needed to pinpoint the exact reason for this effect. Likely contributions include instability in the preloading system, additional charge contributions due to the triboelectric effect, and relaxation effects of the photoelastic media.

Additional testing and optimization is necessary in order to improve accuracy to levels suited for research purposes. It was shown that a highly customizable piezometer, with at least mediocre accuracy, can be built using common laboratory equipment.

I did, however, not manage to test the setup by doing measurements on thin film or nanostructured piezoelectric samples.

Bibliography

[1] Joe Briscoe and Steve Dunn. Piezoelectric nanogenerators – a review of nanostructured piezoelectric energy harvesters. *Nano Energy*, 14:15–29, May 2015.

[2] Zhao Wang, Xumin Pan, Yahua He, Yongming Hu, Haoshuang Gu, and Yu Wang. Piezoelectric Nanowires in Energy Harvesting Applications. *Advances in Materials Science and Engineering*, 2015:1–21, 2015.

[3] Isaku Kanno, Jun Ouyang, Jun Akedo, Takeshi Yoshimura, Barbara Malič, and Paul Muralt. Piezoelectric thin films for MEMS. *Applied Physics Letters*, 122(9):090401, March 2023.

[4] Wenzheng Jiang, Lei Zhu, Lingli Chen, Yumeng Yang, Xi Yu, Xiaolong Li, Zhiqiang Mu, and Wenjie Yu. In Situ Synchrotron XRD Characterization of Piezoelectric Al1xScxN Thin Films for MEMS Applications. *Materials*, 16(5):1781, February 2023.

[5] James M. Gere and Stepan P. Timošenko. *Mechanics of materials*. PWS Publ, Boston, 4. ed edition, 1997.

[6] Jan Tichý, Jiří Erhart, Erwin Kittinger, and Jana Přívratská. *Fundamentals of Piezoelectric Sensorics: Mechanical, Dielectric, and Thermodynamical Properties of Piezoelectric Materials*. Springer Berlin Heidelberg, Berlin, Heidelberg, 2010.

[7] Koichi Hashiguchi. *Elastoplasticity Theory*, volume 69 of *Lecture Notes in Applied and Computational Mechanics*. Springer Berlin Heidelberg, Berlin, Heidelberg, 2014.

[8] IEEE Standard on Piezoelectricity, 1987. ISBN: 9780738124117.

[9] Markys G. Cain. *Characterisation of Ferroelectric Bulk Materials and Thin Films*, volume 2 of *Springer Series in Measurement Science and Technology*. Springer Netherlands, Dordrecht, 2014.

[10] R. S. Weis and T. K. Gaylord. Lithium niobate: Summary of physical properties and crystal structure. *Applied Physics A Solids and Surfaces*, 37(4):191–203, August 1985.

[11] David J. Griffiths. *Introduction to electrodynamics*. Pearson, Boston, fourth edition edition, 2013.

[12] J. M. Liu, B. Pan, H. L. W. Chan, S. N. Zhu, Y. Y. Zhu, and Z. G. Liu. Piezoelectric coefficient measurement of piezoelectric thin films: an overview. *Materials Chemistry and Physics*, 75(1):12–18, April 2002.

[13] Bartłomiej Toroń, Piotr Szperlich, Marian Nowak, and Alicja Starczewska. A novel method for measuring piezoelectric coefficients. *Measurement*, 206:112274, January 2023.

[14] A. Barzegar, D. Damjanovic, and N. Setter. Analytical modeling of the apparent d_{33} piezoelectric coefficient determined by the direct quasistatic method for different boundary conditions. *IEEE Transactions on Ultrasonics, Ferroelectrics and Frequency Control*, 52(11):1897–1903, November 2005.

[15] TE Connectivity. Datasheet FX29 Compact Compression Load Cell, September 2023.

[16] Alessandro Freddi, Giorgio Olmi, and Luca Cristofolini. Introduction to Photoelasticity. In Alessandro Freddi, Giorgio Olmi, and Luca Cristofolini, editors, *Experimental Stress Analysis for Materials and Structures: Stress Analysis Models for Developing Design Methodologies*, Springer Series in Solid and Structural Mechanics, pages 101–165. Springer International Publishing, Cham, 2015.

[17] Andrey G. Paulish, Peter S. Zagubisalo, Vladimir N. Barakov, Mikhail A. Pavlov, and Alexander V. Poyarkov. Piezo-Optical Transducer for High Sensitive Strain Gauges. *IEEE Sensors Journal*, 18(20):8318–8328, October 2018. Conference Name: IEEE Sensors Journal.

[18] Praveen Agarwal, Weijun Zhou, Raghunath Roy, Shih-Wei Chang, and Xiang-Qian Liu. Photoelastic birefringence of copolymers with non-planar structure. *Polymer*, 164:217–222, February 2019.

[19] Ron Mancini. Understanding Basic Analog – Ideal Op Amps. SLaa068B, Texas Instruments, July 1999.

[20] Gustav Gautschi. *Piezoelectric Sensorics*. Springer Berlin Heidelberg, Berlin, Heidelberg, 2002.

[21] Andreas Boes, Lin Chang, Carsten Langrock, Mengjie Yu, Mian Zhang, Qiang Lin, Marko Lončar, Martin Fejer, John Bowers, and Arnan Mitchell. Lithium niobate photonics: Unlocking the electromagnetic spectrum. *Science*, 379(6627):eabj4396, January 2023.

[22] Crystal Technology, Inc. Material Properties Datasheet: Lithium Niobate optical crystals, August 1999.

[23] Stanford Research Systems. About Lock-In Amplifiers.

[24] Matthew Davis, Dragan Damjanovic, and Nava Setter. Direct piezoelectric effect in relaxor-ferroelectric single crystals. *Journal of Applied Physics*, 95(10):5679–5684, May 2004.

[25] Shuaihang Pan and Zhinan Zhang. Fundamental theories and basic principles of triboelectric effect: A review. *Friction*, 7(1):2–17, February 2019.

[26] Desheng Fu Desheng Fu, Kenji Ishikawa Kenji Ishikawa, Makoto Minakata Makoto Minakata, and Hisao Suzuki Hisao Suzuki. Observation of Piezoelectric Relaxation in Ferroelectric Thin Films by Continuous Charge Integration. *Japanese Journal of Applied Physics*, 40(9S):5683, September 2001. Publisher: IOP Publishing.